

**Under-ice acoustic navigation using real-time model-aided range estimation**

EeShan C. Bhatt,<sup>1, 2, a</sup> Oscar Viquez,<sup>2</sup> and Henrik Schmidt<sup>2</sup>

<sup>1</sup>*MIT-WHOI Joint Program in Oceanography/Applied Ocean Science & Engineering,  
Cambridge and Woods Hole, MA, USA*

<sup>2</sup>*Department of Mechanical Engineering, Massachusetts Institute of Technology,  
Cambridge, MA*

(Dated: 21 February 2022)

1 The long baseline (LBL) underwater navigation paradigm relies on the conversion  
2 of recorded travel times into pseudoranges to trilaterate position. For real-time op-  
3 erations, this conversion has assumed an isovelocity sound speed. For re-navigation  
4 in post-processing, computationally and/or labor intensive acoustic modeling may  
5 be employed to reduce uncertainty driven by multipath arrivals. This work demon-  
6 strates a real-time ray-based prediction method of the effective sound speed along  
7 a path from source to receiver to minimize vehicle position error. This method was  
8 implemented for a small scale AUV-LBL system in March 2020, in the Beaufort Sea,  
9 in total ice-covered conditions and a double ducted acoustic propagation environ-  
10 ment. The vehicle was successfully deployed and recovered. Given the lack of GPS  
11 data throughout the vehicle’s mission, however, the pseudorange performance is first  
12 evaluated on connections between GPS-linked beacons. The real-time ranging error  
13 between beacons is roughly 11 meters at distances up to 3 km. But a consistent over-  
14 estimation in the real-time method provides insights for improved eigenray filtering  
15 by the number of surface bounces. An operationally equivalent pipeline is used to  
16 re-position the LBL beacons and re-navigate the AUV, using a modeled, historical,  
17 and a locally observed sound speed profile. The median re-navigation error is  $1.84 \pm 2.19$  RMS m. The improved trilateration performance for suggests that this ap-  
18 proach effectively extends the single meter accuracy of the deployed GNSS units into  
19 the water column.

---

<sup>a</sup>[ebhatt@whoi.edu](mailto:ebhatt@whoi.edu)

<sup>21</sup> **I. INTRODUCTION**

<sup>22</sup> Autonomous underwater vehicles (AUVs) are increasingly capable platforms to explore  
<sup>23</sup> and sample the ocean, particularly for remote and/or dangerous regions. However, navi-  
<sup>24</sup> gation uncertainty is a major challenge in considering AUVs as standard tools for oceano-  
<sup>25</sup> graphic research. While land and air-based robots utilize information from Global Nav-  
<sup>26</sup> igation Satellite Systems (GNSS) to achieve single-meter location accuracy and precision  
<sup>27</sup> throughout the duration of their missions, AUVs cannot access GNSS fixes while under-  
<sup>28</sup> water. Therefore, underwater vehicles have relied on any combination of dead reckoning,  
<sup>29</sup> hydrodynamic models, inertial navigation systems, doppler velocity logs, and acoustic base-  
<sup>30</sup> line positioning systems for navigation ([Paull \*et al.\*, 2014](#)). Limiting navigation error and  
<sup>31</sup> drift requires an AUV to periodically stall on the surface and obtain a GNSS fix to reset its  
<sup>32</sup> position error. This foolproof method of self-positioning is undesirable for stealth, adverse  
<sup>33</sup> weather conditions, and mission efficiency, and inaccessible in a GNSS-denied situation like  
<sup>34</sup> an ice-covered environment.

<sup>35</sup> Of underwater acoustic navigation systems, long baseline (LBL) is the most GPS-like  
<sup>36</sup> in style and scale, and most appropriate for mitigating drift without overburdening com-  
<sup>37</sup> putation or payload size on the vehicle ([Van Uffelen, 2021](#)). The state-of-the-art for LBL  
<sup>38</sup> outsources depth to a pressure sensor and solves the two-dimensional localization problem  
<sup>39</sup> with an isovelocity, linear scaling between one way travel time (OWTT) and range ([Eustice](#)  
<sup>40</sup> *et al.*, 2006, 2007; [Webster \*et al.\*, 2009, 2012](#)). This assumption is valid for short scale op-  
<sup>41</sup> erations but oversimplifies propagation at larger scales or complex sound speed structure.

42 To achieve single meter, GNSS-like performance in a GNSS-denied environment, we demon-  
 43 strate an embedded ray-based data processing algorithm to convert recorded OWTTs into  
 44 pseudorange estimates. This methodology was integrated onto the AUV *Macrura*, deployed  
 45 and recovered in the Beaufort Sea, in March 2020, during the Ice Exercise 2020 (ICEX20).  
 46 A physics-driven methodology that received an *in situ* sound speed profile (SSP) was nec-  
 47 essary despite the small operational domain because of the relatively high-risk mission en-  
 48 vironment—total under-ice conditions and a variable double ducted acoustic environment.  
 49 For consistency, we delineate specific definitions for timing, positioning, and navigation  
 50 from [Howe et al. \(2019\)](#).

- 51     1. Timing is the ability to acquire and maintain accurate and precise time anywhere in  
 52         the domain of interest within user-defined timeliness parameters
- 53     2. Positioning is the ability to accurately and precisely determine one's location refer-  
 54         enced to a standard geodetic system
- 55     3. Navigation is the ability to determine current and desired position (relative or absolute)  
 56         and apply corrections to course, orientation, and speed to attain a desired position  
 57         anywhere in the domain of concern

58 Thus, navigation is inherently in real-time and depends on positioning; positioning depends  
 59 on timing. We also suggest re-navigation and re-positioning as post-processed corollaries,  
 60 which may include knowledge or processing capabilities not available *in situ*.

61     While RAFOS floats championed one way ranging for re-positioning ([Duda et al., 2006](#);  
 62 [Rossby et al., 1986](#)), the ability to do so for navigation was facilitated by the advent of

63 the WHOI Micro-Modem (Singh *et al.*, 2006) and synchronized clocks (Rypkema *et al.*,  
64 2017). AUV navigation efforts have achieved root mean square (RMS) localization error on  
65 the order of tens of meters relative to GNSS surface position over less than ten kilometers  
66 in shallow (Claus *et al.*, 2018; Eustice *et al.*, 2007; Kepper *et al.*, 2017) and deep water  
67 (Jakuba *et al.*, 2008; Kunz *et al.*, 2008; Webster *et al.*, 2009). However, these efforts all used  
68 a nominal sound speed for travel time conversion and the vehicles were limited to shallower  
69 isovelocity regimes.

70 Localization algorithms that do consider environmental or acoustic uncertainty tend to  
71 focus on longer duration and larger range experiments, where spatio-temporal variability  
72 cannot be ignored. These methods have also been reserved for post-processing as they  
73 can be labor intensive, computationally heavy, and/or require additional information like  
74 contemporaneous data. For example, gliders navigating with kinematic flight models and  
75 equipped with acoustic modems were later unambiguously associated with predicted ray  
76 arrivals, resulting in roughly a kilometer error and hundred meters uncertainty over basin  
77 scale propagation (Van Uffelen *et al.*, 2013). A follow up study investigated how a single  
78 temporally and spatially averaged SSP could mitigate position error for a four month glider  
79 mission (Van Uffelen *et al.*, 2016). Wu *et al.* (2019) cross correlate three days of real acous-  
80 tic records with synthetic ones generated through ocean model snapshots from HYCOM  
81 (Chassagnet *et al.*, 2007). While potentially applicable for various ocean states, this is re-  
82 liant on model realism and impractical for real-time operations. A “cold start” algorithm  
83 that does not require prior knowledge of track, position, or sound speed information inputs  
84 a four-dimensional ocean model, constrained by tomography data, into a range dependent

85 ray code to isolate the last path detected in a full multipath pattern (Mikhalevsky *et al.*,  
86 2020). Then, a representative group speed is solved for alongside position in a least squares  
87 fashion. This approach is able to re-position a floating hydrophone array with an error of  
88 58 m and a standard deviation of 32 m based on six sources 129–450 km away but remains  
89 to seen for real-time navigation.

90 The ICEX20 AUV deployment necessitated an environmentally- and physically-driven  
91 relationship between recorded travel times and estimated pseudoranges due to the multipath  
92 uncertainty brought upon by an increasingly observed double ducted environment in the  
93 Beaufort Sea, which some refer to as the “Beaufort Lens” (Chen *et al.*, 2019; Chen and  
94 Schmidt, 2020; Litvak, 2015).

95 Given that a lens introduces significant ray refraction, the Beaufort Lens is a shorthand for  
96 the spatio-temporal variability of the local temperature and sound speed maxima generally  
97 around 50 to 60 m in depth. A neutrally buoyant layer of warm Pacific Summer Water  
98 creates a unique double ducted environment —the upper duct degrades signal coherence  
99 due to intensified ice interaction and the lower duct effectively traps sound for long range  
100 propagation (Poulsen and Schmidt, 2017). Modeling output (Duda *et al.*, 2021, 2019) and  
101 experimental observations (Ballard *et al.*, 2020; Bhatt, 2021) suggest that, in the Beaufort  
102 Sea, the duct is persistent and widespread but not necessarily continuous; it and its acoustic  
103 effects can be non-existent, minimal, or drastic. Transmissions in the upper duct, between  
104 the surface ice and the lens, experience minimal attenuation but degrade in signal coherence  
105 with repeated reflections under the ice. In the lower duct, between the lens and its conjugate

<sup>106</sup> depth in the Atlantic water (roughly 200 m), sound above 350 Hz is trapped near losslessly  
<sup>107</sup> for long range propagation (Poulsen and Schmidt, 2017).

<sup>108</sup> The Arctic, while remote, is the perfect place to demonstrate mature navigation tech-  
<sup>109</sup> nologies in real GNSS-denied conditions. Thorough reviews of uncrewed vehicle operations  
<sup>110</sup> in polar environments can be found in Norgren *et al.* (2014) and Barker *et al.* (2020); there  
<sup>111</sup> is no comparable work in the Arctic for a short range AUV deployment in the Beaufort  
<sup>112</sup> Lens. Seminal Arctic AUV deployments (Bellingham *et al.*, 1995; Brooke, 1981; Hayes and  
<sup>113</sup> Morison, 2002; Jackson, 1983; Light and Morison, 1989) and more recent ones (Fossum  
<sup>114</sup> *et al.*, 2021; Jakuba *et al.*, 2008; Kukulya *et al.*, 2010; Kunz *et al.*, 2008; Plueddemann *et al.*,  
<sup>115</sup> 2012; Timmermans and Winsor, 2013) witnessed the classical upward refracting sound speed  
<sup>116</sup> profile that is amenable to an isovelocity assumption.

<sup>117</sup> Of note, despite different platforms and scales, are recent glider deployments in the  
<sup>118</sup> Canada Basin. In 2014, in partially ice-covered conditions, a long range LBL system with  
<sup>119</sup> WHOI Micro-Modems at 100 m depth exploited the lower duct for long range communication  
<sup>120</sup> with two gliders (Freitag *et al.*, 2016; Webster *et al.*, 2015). The sound speed value measured  
<sup>121</sup> at the time of reception was used to estimate pseudorange in post-processing. The beacon-  
<sup>122</sup> to-beacon performance was excellent, achieving contact at ranges greater than 200 km with  
<sup>123</sup> a position uncertainty of 40 m. The beacon-to-glider performance, however, deteriorated  
<sup>124</sup> due to missed contacts outside the duct, and was not described quantitatively. In 2017,  
<sup>125</sup> gliders were deployed in a region with no ice coverage (Graupe *et al.*, 2019). Ranges were  
<sup>126</sup> linearly scaled by a statistical description of sound speed observations taken during the  
<sup>127</sup> experiment,  $1450 \pm 6.5$  m/s. This resulted in an error of 550 m, which was reduced by

128 a factor between 4 and 5, depending on the dive, using a post-processing acoustic arrival  
129 matching method. Both cases exploit the lower duct for high fidelity communication at long  
130 ranges. Unintuitively, the smaller scale nature of our deployment during ICEX20 is not a  
131 simplifying factor. For source depths typical to vehicle operations, 30 to 200 m, the Beaufort  
132 Lens introduces a shadow zone that spans from 2 to 6 kilometers in range ([Schmidt and](#)  
133 [Schneider, 2016](#)).

134 Compared to previous small scale navigation efforts, the approach in this paper integrates  
135 real-time model-aided data processing to estimate a representative sound speed along a path  
136 from source to receiver, leveraging climatology, *in situ* data, and fast acoustic modeling. The  
137 paper is organized as follows. Section [II](#) details the experimental approach and conditions  
138 during ICEX20. Given that there is no GNSS ground truth for the vehicle position while  
139 underway, we first evaluate the real-time ranging performance of GPS-linked beacon-to-  
140 beacon communication events in section [III](#). Section [IV](#) uses insights from field data to  
141 introduce a new ray filtering algorithm to improve range estimation. Section [V](#) emulates the  
142 real-time processing pipeline to re-position beacon-to-beacon events and re-navigate AUV  
143 *Macrura*.

<sup>144</sup> **II. OVERVIEW OF THE ICEX20 EXPERIMENT**

<sup>145</sup> The results from this paper derive from data collected while deploying the AUV *Macrura*,  
<sup>146</sup> a custom Bluefin-21, during the Ice Exercise 2020 (ICEX20). The experiment was conducted  
<sup>147</sup> in the Beaufort Sea, from March 8th to 11th, at roughly 71.2°N. The AUV deployment was  
<sup>148</sup> supported by the Integrated Communication and Navigation Network (ICNN) ([Randeni](#)  
<sup>149</sup> *et al.*, 2020, 2021; [Schneider et al.](#), 2021) a specialized implementation of the LBL solution.  
<sup>150</sup> The ICNN was initially developed via numerous virtual experiments to ensure robust algo-  
<sup>151</sup> rithms and interfaces between different hardware components. The simulation capabilities  
<sup>152</sup> are largely physics-driven with a modular system of systems approach—an environmental  
<sup>153</sup> simulator with sub-components for the ocean, including Arctic ice drift and ocean acoustic  
<sup>154</sup> propagation; a vehicle simulator with sub-components for vehicle dynamics and navigation;  
<sup>155</sup> a topside hardware simulator and acoustic communications simulator, both with a software-  
<sup>156</sup> only configuration and a hardware-in-the-loop version ([Schneider and Schmidt](#), 2018). The  
<sup>157</sup> virtual environment similarly emulates the interfaces between the real components to test  
<sup>158</sup> the entire software pipeline.

<sup>159</sup> **A. The Integrated Communication and Navigation Network**

<sup>160</sup> The ICNN is comprised of four ice buoys in a loose rectangle, roughly 2 km away from  
<sup>161</sup> a central ice camp with a topside computer, as shown in Fig. 1. Each ice buoy is outfitted  
<sup>162</sup> with a Garmin GPS 18x, with a pulse-per-second rising edge aligned to 1 microsecond and  
<sup>163</sup> a spec sheet accuracy of 3 m, 95% of the time. They are also each equipped with a WHOI

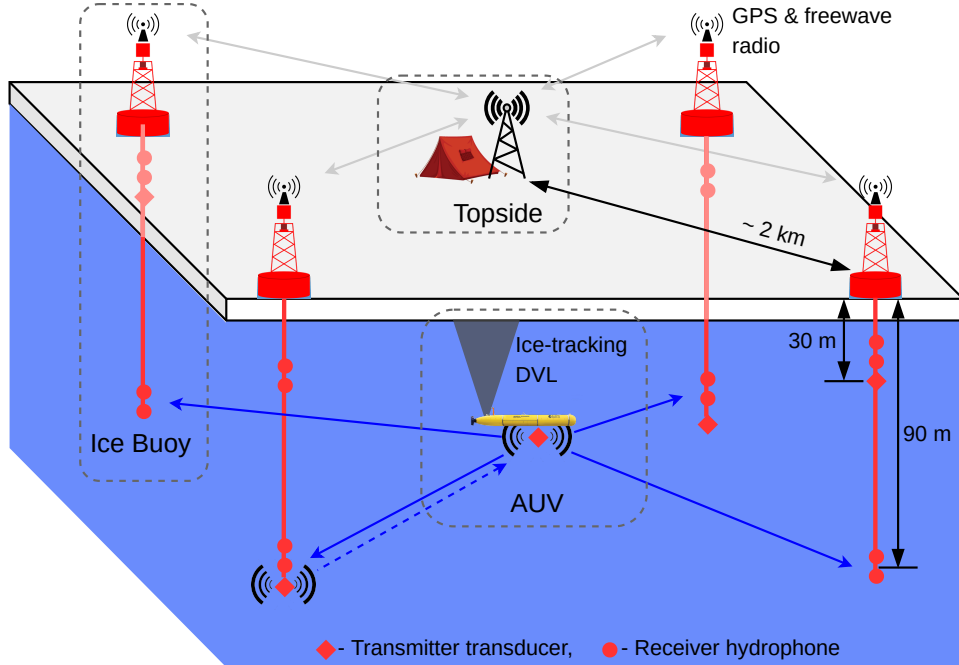


FIG. 1. A schematic overview of the Integrated Communication and Navigation Network (ICNN), which provides joint data-transfer and tracking between AUV and a human decision maker at Topside.

164 Micro-Modem ([Singh \*et al.\*, 2006](#)), with a four-element receiver array, a single transmitter,  
 165 and one-tenth of a millisecond resolution. Acoustic messages were sent with a 10 kHz carrier  
 166 frequency, 5 kHz bandwidth, and phase-shift keying (PSK) modulation on a time-division  
 167 multiple access schedule with a thirty-second cycle, giving room for two-way communication  
 168 throughout the mission volume. Thus the ICNN is dependent on the successful decoding of  
 169 acoustic transmissions. The receive and transmit elements were split between shallow and  
 170 deeper depths—30 and 90 m—to provide better coverage across the shadow zone. While  
 171 each buoy only has one transmit depth, all buoys have both receive depths but the active  
 172 receive layer is consistent across all buoys. The design of the ICNN enables a self-adapting

173 network to transmit and receive at the optimal depth to maintain contact with the AUV  
 174 (Schneider *et al.*, 2021). The buoys do not encompass the full horizontal range of the vehicle  
 175 but are positioned to minimize overlap in trilateration for spherical positioning (Deffenbaugh  
 176 *et al.*, 1996a).

177 To balance competing uses of the acoustic channel, the network uses a single synchronized  
 178 digital communication packet to provide both tracking and data to the operator.

179 1. The AUV, running an ice-tracking DVL and an onboard hydrodynamic model, broad-  
 180 casts its perceived location on a scheduled, time-synchronized message via WHOI  
 181 Micro-Modem

182 2. Four ice buoys, each outfitted with a WHOI Micro-Modem, receive messages from the  
 183 AUV and send that information over freewave radio to a Topside computer

184 3. The topside computer converts travel times into pseudorange estimates using a stochas-  
 185 tic embedded prediction of the horizontal group velocity via BELLHOP ray tracing  
 186 code (Porter, 2011) using a sound speed profile provided by an updatable Virtual  
 187 Ocean (Bhatt *et al.*, 2022; Schneider and Schmidt, 2018)

188 4. The topside computer calculates a new position by trilaterating the range estimates  
 189 5. The position differential, not the absolute position, is broadcast to the vehicle to  
 190 update its navigation solution and be robust to latency and intermittency

191 In the face of GNSS-denied navigation, this approach was anecdotally successful, as shown  
 192 in Fig. 2. The AUV *Macrura* was deployed through a hydrohole from an ice camp but re-  
 193 covered through an emergency hydrohole. A random disk error stalled *Macrura* underneath

194 the ice but did not prevent it from transmitting its location. Due to an incoming storm, a  
 195 team drilled an exploratory hole at *Macrura*'s self-reported location, and were able to drill a  
 196 separate hole 1 m away to tie the vehicle off to a physical marker on the ice. Three days later,  
 197 *Macrura* was recovered—the ice camp had moved over 19 km. The AUV's relative position  
 198 to camp had also changed, from roughly 45°at 1000 m to 90°at 1100 m. Drama aside, we view  
 199 the emergency recovery as qualitative proof of the robustness of this navigation approach.  
 200 Nonetheless, this paper specifically addresses the third and fourth steps—the conversion  
 201 of travel times into pseudoranges and its quantitative effect on trilateration. By focusing  
 202 on pseudorange estimates between GPS-tracked beacons, and re-running the trilateration  
 203 pipeline, the results are decoupled from all other mechanisms in the ICNN.

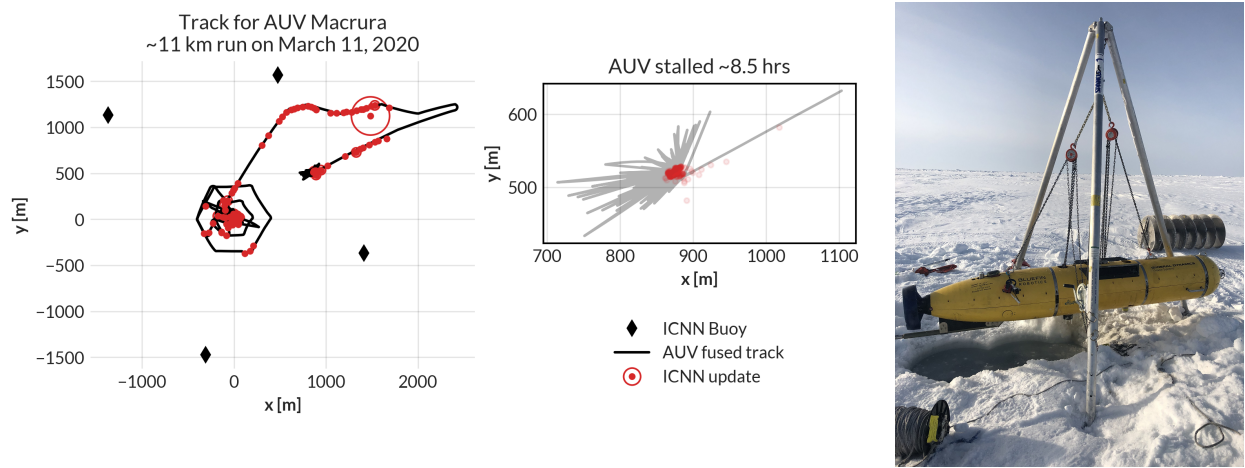


FIG. 2. The under-ice mission track for AUV *Macrura*, including the position updates as it stalled underneath the ice overnight. A marker was placed on the ice at the vehicle's estimated self-location. It was recovered after a three day storm within a meter of the marker.

204      **B. ICEX20 sound speed conditions**

205      An important component to our navigation solution is an accurate estimation of a repre-  
 206      sentative SSP for the ocean volume. Previous field experience, during the Ice Exercise 2016  
 207      (ICEX16), demonstrated the negative effects of the Beaufort Lens on tracking and commu-  
 208      nication (Schmidt and Schneider, 2016). Fig. 3 shows historical, modeled, and *in situ* sound  
 209      speed data for both ICEX16 and ICEX20. These three input streams were selected to mirror  
 210      the information available on a submarine (personal conversation with LT B. Howard and LT  
 211      CDR D. Goodwin). In the field, the SSP information was shared with the vehicle via basis  
 212      representation compression on a lightweight digital acoustic message (Bhatt *et al.*, 2022).  
 213      All modeled data comes from HYCOM (Chassagnet *et al.*, 2007), which does not seem to  
 214      capture the forcing mechanisms that cause the Beaufort Lens. For ICEX16, the data-driven  
 215      profile was sourced from nearby Ice Tethered Profilers (ITP) after the field experiment (Kr-  
 216      ishfield *et al.*, 2008; Toole *et al.*, 2011) and exhibits a fairly deep lens; the historical profile is  
 217      from the World Ocean Atlas. For ICEX20, the chosen weights (data-driven) profile derives  
 218      from initial CTD casts taken on site, showing an intense warm water intrusion; the baseline  
 219      (historical) profile, showing moderate ducted conditions, comes from the average of March  
 220      2013 ITP data. This month best matched sea ice and sound speed conditions at the begin-  
 221      ning of ICEX20 (Bhatt *et al.*, 2022). It is important to note that all profiles that do show the  
 222      Beaufort Lens do so with different local sound speed maxima at different depths, reflective  
 223      of the wide range of lens properties observed for all ITP data in the region. The variability

<sup>224</sup> of the lens height and prominence is the main reason an updatable SSP was integrated into  
<sup>225</sup> the ICNN solution.

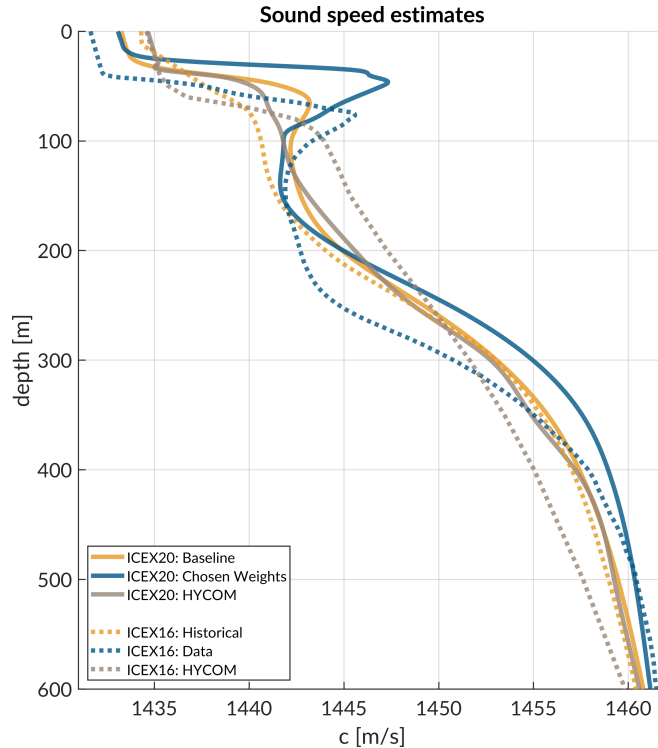


FIG. 3. Sound speed conditions for historical (baseline), data (chosen weights), and HYCOM model for both ICEX16 and ICEX20.

<sup>226</sup> During ICEX20, the HYCOM profile was available but never deployed. For post-  
<sup>227</sup> processing comparison, we introduce both the HYCOM profile and an isovelocity case,  
<sup>228</sup>  $1441.8 \pm 3.7$  m/s, as the mean and standard deviation of the observed sound speed profile  
<sup>229</sup> over the first 200 m. This is a contrived value taken in the style of [Graupe et al. \(2019\)](#)  
<sup>230</sup> for the sake of comparison; the default value in the LAMSS simulator, which was not envi-  
<sup>231</sup> ronmentally informed and used when no updates were available from the ICNN, was 1430  
<sup>232</sup> m/s.

233 **III. REAL-TIME PSEUDORANGE ANALYSIS**

234 Because the vehicle’s navigation solution during a mission can only be evaluated on the  
235 basis of the error estimates sent, a sister experiment for validating the real-time ranging  
236 approach was implemented. Ice buoy modems were run as “virtual vehicles” at a fixed  
237 depth, receiving position updates from the other beacons as well as a camp site modem  
238 lowered to 20 m. Fig. 4 shows successful events sorted by source depth. In this analysis, we  
239 assume there is insignificant displacement between the GNSS puck surface expression and  
240 subsurface modem; this is supported by unusually low observed ice drift rates, just 0.7 cm/s  
241 on average throughout the mission.

242 **A. Minimal bounce (MB) criteria**

243 The fundamental challenge to implement GNSS-like navigation, especially in an acousti-  
244 cally complex propagation environment, is characterizing a single sound speed to compensate  
245 for the effects of ray refraction and reflection. The use of the acoustic modem network for  
246 tracking relies on the accurate estimation of travel times between the submerged platform  
247 and LBL beacons, supported by clock synchronization and a pre-determined scheduling of  
248 acoustic events. For the Beaufort Lens in particular, the strong multipath effects make it  
249 virtually impossible to deterministically predict the modem’s detected arrival time.

250 Instead, for each individual receiver  $i$ , an embedded stochastic tracking framework is used  
251 to provide a running estimate of the effective sound speed  $c_{i,j}$  for the conversion from travel  
252 time to range from modem  $j$ , with the ultimate goal of matching the implied horizontal

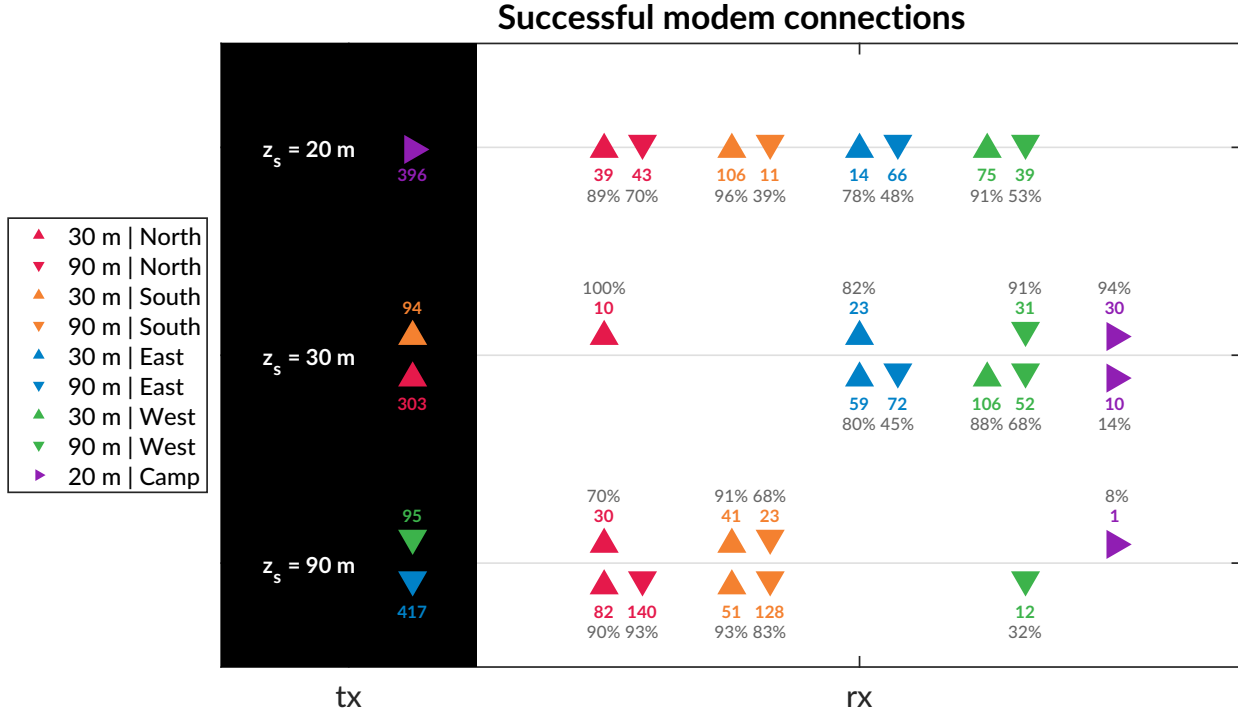


FIG. 4. An overview of the modem experiment by source and receiver depth and position. The black column on the left, *tx*, shows the source depth,  $z_s$ , with the total number of transmissions. The column on the right, *rx*, shows the receivers with the number of successful decodings and the percent success rate, defined as the ratio of decoded to detected. The orientation of the triangles—sideways, upwards, and downwards—corresponds to depths of 20, 30, and 90 m.

253 effective sound speed, i.e., the GPS-recorded distance between two nodes divided by the  
 254 modem-recorded one way travel time between them.

255 In the ICEX20 configuration, the acoustic tracker is running on the topside computer,  
 256 which controls the ICNN. Here we assume that the effective sound speeds  $c_{i,j}$  are smoothly

257 varying over the course of a vehicle mission, i.e., with respect to range from signal origin at  
 258 transmitter  $j$ , mission time, and the thirty-second frequency.

259 When the topside tracking framework receives a message, with a time delay,  $\Delta t$ , it will  
 260 request a new estimate for  $c_{i,j}$  along with its standard deviation. The effective sound speed  
 261 is predicted using the vehicle's reported depth and the extrapolated navigation solution for  
 262 range,  $\hat{r}$ , as inputs to the ray tracing program, which returns an impulse response estimate  
 263 in the form of ray travel times  $dt_j$  and amplitudes  $a_j$ .

264 The initial call to BELLHOP is over a local grid centered at the range and depth posited  
 265 by the onboard tracking solution. The grid, compared to a point solver, adds redundancy  
 266 in resolving the actual multipath structure for a reliable acoustic path without overtaxing  
 267 onboard computational time and memory. It is initialized as  $11 \times 11$  points spanning 10  
 268 m horizontally and 20 m vertically. The horizontal dimension reflects the accumulated  
 269 vehicle position error given a thirty-second communication cycle; the vertical dimension  
 270 reflects how, computationally, eigenrays of the same timefront seem to stack vertically in  
 271 the water column. For each grid point, BELLHOP produces a number of arrivals resulting  
 272 from multiple propagation paths. Using only the  $N_0$  rays with neither surface nor bottom  
 273 bounces, the tracking system will then estimate the current effective sound speed  $c$  from a  
 274 power weighted average of the ray travel times,

$$c = \frac{\hat{r} \sum_{n=1}^{N_0} a_n^2}{\sum_{n=1}^{N_0} dt_n a_n^2}, \quad (1)$$

275 and the associated weighted standard deviation,

$$\sigma_c \simeq \sqrt{\frac{\sum_{n=1}^{N_0} (dt_n - \hat{r}/u)^2 a_n^2}{\sum_{n=1}^{N_0} a_n^2}} \frac{u^2}{\hat{r}} \quad (2)$$

<sup>276</sup> If no direct paths exist, i.e.  $N_0 = 0$ , then the effective speed is computed using the same  
<sup>277</sup> algorithm for the ray arrivals with one bounce, and so on.

<sup>278</sup> Finally, the pseudorange is calculated simply as

$$r_{i,j} = c_{i,j} \Delta t_{i,j} \quad (3)$$

<sup>279</sup> Thus the minimal bounce (MB) criteria assumes the signal detected by the modem will  
<sup>280</sup> be dominated by a set of paths with the least number of boundary interactions. Impor-  
<sup>281</sup> tantly, this stochastic, ensemble method for group velocity calculation can run in real-time,  
<sup>282</sup> appearing to be orders of magnitude faster than other post-processing methods which seek  
<sup>283</sup> to determine the specific ray itself that best matches a prominent indicator from the arrival  
<sup>284</sup> structure. The BELLHOP simulation that runs this calculation uses 3600 rays with launch  
<sup>285</sup> angle fan of -60 to 60 degrees, a representative depth dependent sound speed profile, and a  
<sup>286</sup> range dependent bathymetry.

<sup>287</sup> **B. Pseudorange error metrics**

<sup>288</sup> The sister modem experiment generated 811 beacon to beacon communication events  
<sup>289</sup> with their own effective sound speed predictions from a real-time implementation of the  
<sup>290</sup> MB method. Given the complexity of the ICNN system, this experiment did not collect an  
<sup>291</sup> exhaustive set of data across all buoy, source depth, receive depth, and model sound speed  
<sup>292</sup> combinations. The algorithm generally overestimates pseudoranges because it resolves the  
<sup>293</sup> effective sound speed for the most direct path.

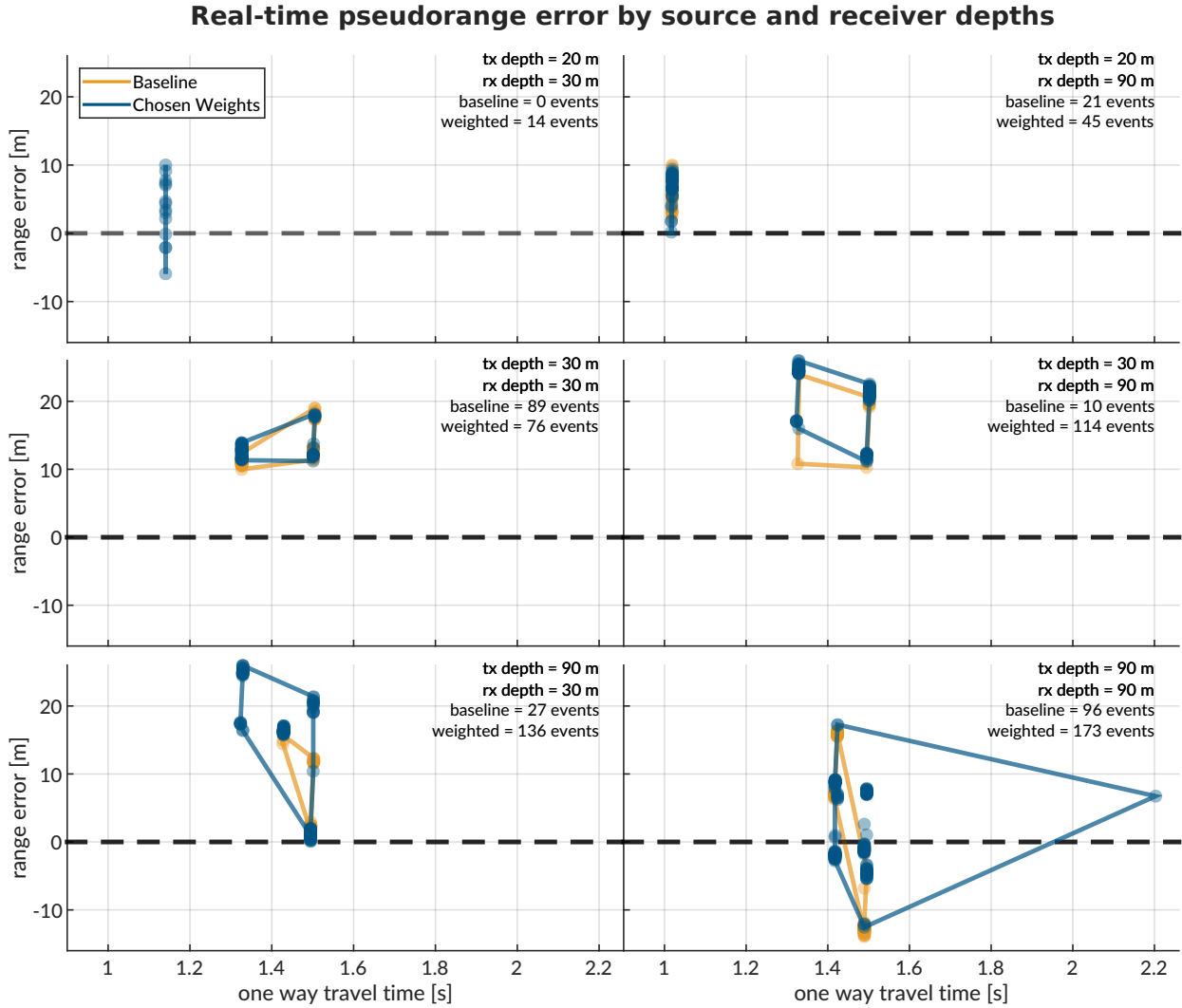


FIG. 5. The real-time range error by source (rows: 20, 30, and 90 m) and receiver (columns: 30 and 90 m) pairings for both sound speed estimates used during ICEX20. The amount of communication events is notated in the top right of each panel. The dashed line indicates no range error, and the boundary drawn indicates scope of the range error as a function of one way travel time.

Fig. 5 shows the range error boundary for both SSP inputs used in ICEX20. A promising sign that the MB method adapts sound speed somewhat intelligently is the lack of error growth as travel time increases. The baseline SSP ( $n=243$  events) has an absolute pseudor-

297 range error of  $11.38 \pm 4.23$  m; the weighted SSP ( $n=568$ ),  $11.36 \pm 8.12$  m. The discrepancy  
 298 between these two is largely due to outlier events only contained in the weighted SSP set.  
 299 Where there is overlap between sound speed conditions used for the real-time MB approach,  
 300 the pseudorange error difference is no more than a few meters. The overarching results show  
 301 that sound speed estimates derived from eigenrays for a local grid, as opposed to a singular  
 302 point, are accurate enough to support vehicle navigation. While the MB looks for just the  
 303 least complex multipath, the high density of launch angles almost always guarantees a direct  
 304 path for the beacon-to-beacon configurations. Nonetheless, the consistent overestimation of  
 305 pseudorange invites further analysis into acoustic arrival matching.

### 306 C. Eigenray identification for beacon-to-beacon events

307

308 Accounting for ice movement between beacons creates nominal ranges with small vari-  
 309 ability. Figs. 6, 7, and 8 show eigenrays for three sound speed environments for source  
 310 depths of 20, 30, and 90 m, respectively. Eigenrays were initially found using the built-in  
 311 BELLHOP protocol with a launch angle fan of 2400 rays between -60 and 60 degrees. Sepa-  
 312 rately, recorded travel times between beacons were clustered with 1 millisecond boundaries  
 313 such that some source-receiver pairs had multiple, distinct travel times to approximate. The  
 314 BELLHOP eigenray returns were then filtered such that one was selected per travel time  
 315 cluster, in the hopes that the eigenray will converge to the receiver locations for the most  
 316 realistic sound speed input. It should be noted that bottom bounces were recovered but

<sup>317</sup> filtered out. The three source depths create distinct ray geometries with respect to the three  
<sup>318</sup> sound speed inputs.

<sup>319</sup> **1. Source depth of 20 m**

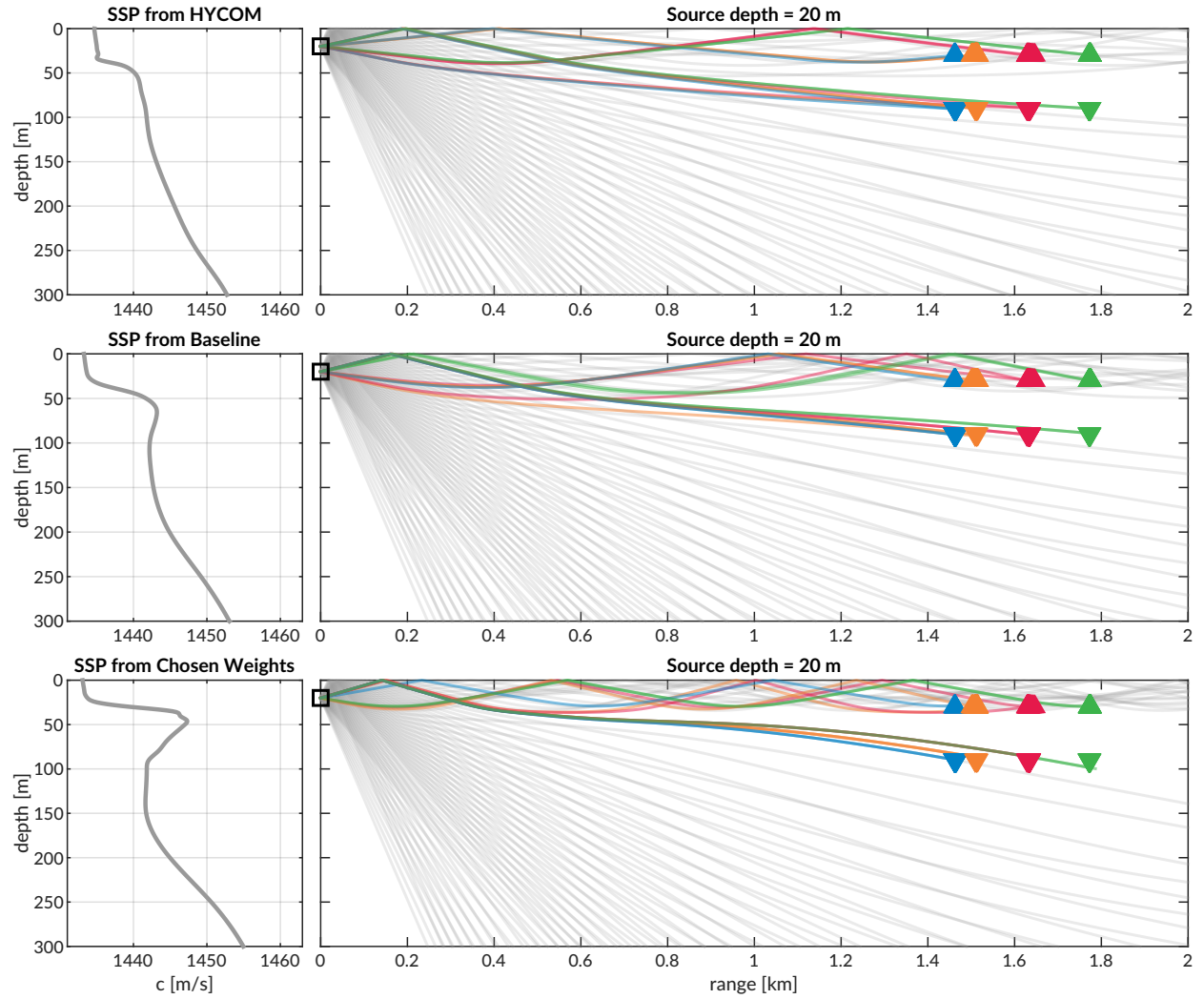


FIG. 6. Eigenrays for beacon-to-beacon events for each sound speed with a nominal source depth of 20 m over a total ray fan in gray. The beacons are highlighted in color/marker coding in Fig. 4.

320 For a source at 20 m in depth, shown in Fig. 6, reliable eigenrays are found for all sound  
 321 speed inputs. Rays refract upwards and neatly intersect with the shallow and deep receiver  
 322 locations between 1.5 and 1.8 km in range. However, the ray paths for the shallow receivers  
 323 change both in the number of surface interactions and where the surface interactions occur  
 324 with respect to range across the SSPs. As the Beaufort Lens strengthens, the chosen paths to  
 325 the second farthest shallow buoy (North, in red) interact with the surface more and become  
 326 distinct. The weighted SSP shows the most interesting effects for the deeper receivers. The  
 327 ray paths all interact with the surface and the eigenrays for the Northern (red) and Western  
 328 (green) buoys are in fact the same ray.

## 329 ***2. Source depth of 30 m***

330 The ray geometries from the 30 m source, shown in Fig. 6, show a similar degradation of  
 331 eigenray identification with increased ducting. Receptions span 1.5 to 3.2 km. Once again,  
 332 eigenrays for HYCOM and the baseline SSP are visually appropriate. Rays for the weighted  
 333 SSP show how the surface channel intensifies ice interactions and how the shadow zone denies  
 334 reliable acoustic paths. Pointedly, the increasing number of surface reflections to the farthest  
 335 shallow buoy (North, in red) crystallize the MB criteria's tendency for overestimation. For  
 336 the HYCOM, baseline, and weighted SSP inputs, the most appropriate eigenrays show 2, 3,  
 337 and 4 surface interactions.

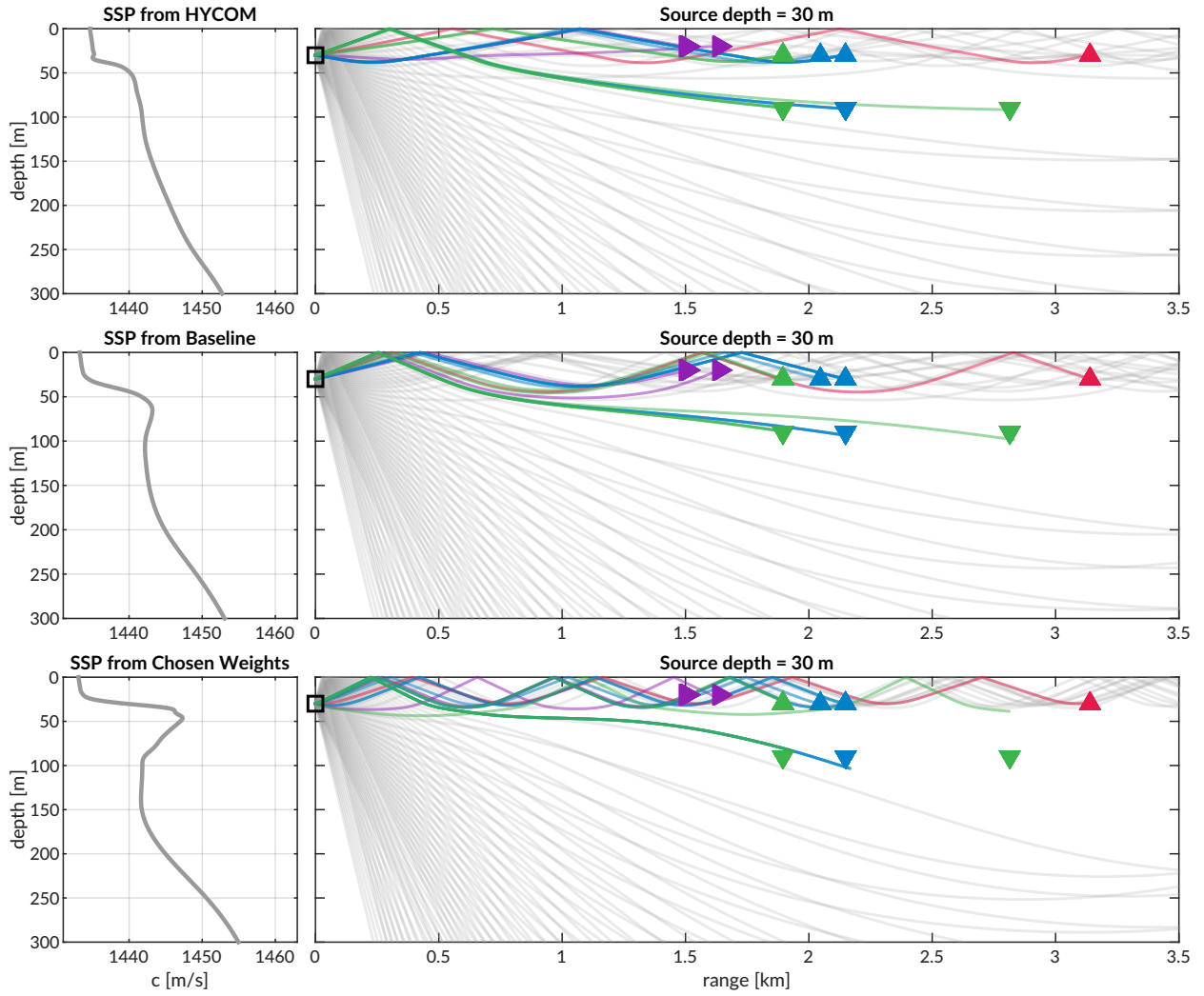


FIG. 7. Eigenrays for beacon-to-beacon events for each sound speed with a nominal source depth of 30 m over a total ray fan in gray. The beacons are highlighted in color/marker coding in Fig. 4.

<sup>338</sup>      **3. Source depth of 90 m**

<sup>339</sup>      Lastly, Fig. 8 shows ray geometries from the 90 m source, elucidating a different extent  
<sup>340</sup> of the shadow zone. While the receiver locations are similar to that of the 30 m source  
<sup>341</sup> depth, the deeper source depth effectively negates the upper duct and places the upper (and  
<sup>342</sup> some of the lower) receivers in unreliable acoustic paths. The HYCOM eigenrays still show

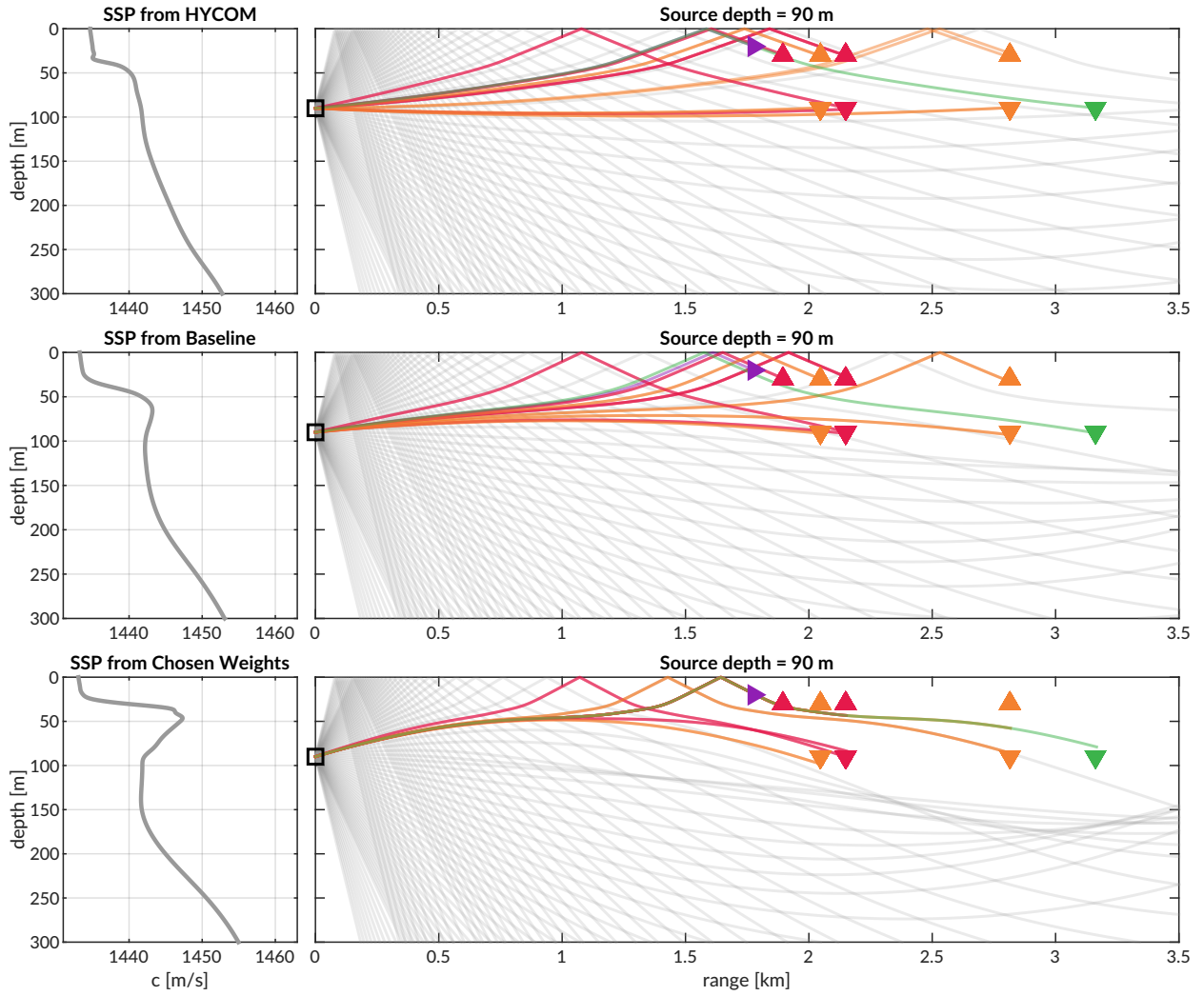


FIG. 8. Eigenrays for beacon-to-beacon events for each sound speed with a nominal source depth of 90 m over a total ray fan in gray. The beacons are highlighted in color/marker coding in Fig. 4.

343 the most reliable acoustic paths that deteriorate with increasing ducted conditions. The  
 344 lack of direct paths from the observed SSP further points out the shortcomings of the MB  
 345 approach.

346 The goal of the MB algorithm was to provide a reliable, physically intuitive interpretation  
 347 of the acoustic propagation without taking on the additional burden of regularly identifying  
 348 specific paths that may connect any given source-receiver pair in the network. While it

349 was unlikely to resolve multipath arrivals that triggered successful modem detection, an  
350 isovelocity approach would have provided no adaptivity against source and receiver depth  
351 differences. Its performance was adequate for vehicle navigation and would have likely  
352 sufficed if it were not for the prominence of the duct observed relative that of other model  
353 and data products.

<sup>354</sup> **IV. POST-PROCESSED PSEUDORANGE ANALYSIS**

<sup>355</sup> From all events recorded during the modem test experiment, there are 1242 successfully  
<sup>356</sup> decoded beacon-to-beacon events. Thus, a post-processing analysis that emulates the real-  
<sup>357</sup> time navigation engine was run to overcome the unequal distribution of communication  
<sup>358</sup> events with respect to depth, range, and sound speed status.

<sup>359</sup> It is important to note that the value for the extrapolated range,  $\hat{r}$ , is only tracked by  
<sup>360</sup> topside for a modem claiming to be the vehicle; thus we replace  $\hat{r}$  with the GPS-tracked range  
<sup>361</sup> for all modem events. Because  $\hat{r}$  converges to the correct solution, a comparison of  $\hat{r}$  with  
<sup>362</sup> the GPS-tracked range shows a normal, zero-centered distribution within the bounds of GPS  
<sup>363</sup> drift. The analysis therefore seeds realistic but “omniscient” knowledge of the extrapolated  
<sup>364</sup> range and emulates the post-processing pipeline to more thoroughly evaluate the acoustic  
<sup>365</sup> pseudorange estimate for all modem events. Sound speed inputs are the isovelocity sound  
<sup>366</sup> speed in addition to the modeled, baseline, and weighted SSPs from Fig. 3. The analysis  
<sup>367</sup> replicates the MB criteria but also introduces a new filtering algorithm, the nearest bounce  
<sup>368</sup> (NB), based on insights gleaned from the eigenray analysis. Accordingly, the results in this  
<sup>369</sup> section evaluate the utility of the algorithms and sound speed sources, divorced from their  
<sup>370</sup> role in the ICNN while maintaining real-time relevance.

<sup>371</sup> **A. Nearest bounce (NB) criteria**

<sup>372</sup> The extent of ray bending and repeated reflections is extremely dependent on the degree of  
<sup>373</sup> the Beaufort Lens observed. Based on this insight, a new algorithm, the nearest bounce (NB)

<sup>374</sup> criteria, is a slight modification from the MB and includes multipath as a new dimension of  
<sup>375</sup> information to exploit. This metric, while run in post-processing, adds a negligible amount  
<sup>376</sup> of computation for real-time efficacy.

<sup>377</sup> Given a running estimate for the effective sound speed  $c_{i,j}$  between nodes  $i$  and  $j$ , the  
<sup>378</sup> navigation system has an extrapolated value for range,  $\hat{r}$ , and a recorded travel time,  $\Delta t_{i,j}$ .  
<sup>379</sup> Instead of using only the  $N_0$  rays with neither surface nor bottom bounces to estimate  
<sup>380</sup> conversion speed, and subsequently moving to incremental number of bounces only when no  
<sup>381</sup> valid direct path solutions exist, we solve for the power weighted average of the ray travel  
<sup>382</sup> time for the  $N_k$  rays with  $k$  bounces,

$$t_k = \frac{\sum_{n=1}^{N_k} dt_n a_n^2}{\sum_{n=1}^{N_k} a_n^2}, \quad (4)$$

<sup>383</sup> find the nearest matching power weighted average to recorded travel time,

$$t_{i,j,k} = \min_{k=0,1,2,\dots} |t_k - \Delta t_{i,j}| \quad (5)$$

<sup>384</sup> predict an effective sound speed,

$$c_{i,j} = \frac{\hat{r}}{t_{i,j,k}} \quad (6)$$

<sup>385</sup> and estimate the range as was done previously.

$$r_{i,j} = c_{i,j} \Delta t_{i,j} \quad (7)$$

<sup>386</sup> Whereas the MB outputs a scalar, this method first outputs a vector of effective sound  
<sup>387</sup> speeds based on the number of reflections. Then a single value is selected in a nearest-  
<sup>388</sup> neighbor fashion that best matches the recorded travel time, as the detected arrival is not  
<sup>389</sup> always the first arrival or the direct path and could even be masked by noise or blocked

<sup>390</sup> temporarily (Deffenbaugh *et al.*, 1996b). We manually cap the number of bounces at four  
<sup>391</sup> because of the smaller operational scale and the attenuation accrued with many surface  
<sup>392</sup> interactions. Bottom bounces are not encoded separately because ray's tendency to  
<sup>393</sup> refract upward, not due to information limitations.

<sup>394</sup> **B. Effective sound speed predictions**

<sup>395</sup> The minimal and nearest bounce algorithms are applied with the three sound speed inputs  
<sup>396</sup> shown in Figs. 6, 7, 8. The resulting predicted effective sound speeds are shown in Fig. 9  
<sup>397</sup> for all source depths versus one way travel time.

<sup>398</sup> The goal of the effective sound speed prediction is to converge towards the implied sound  
<sup>399</sup> speed, i.e. the GNSS-derived range divided by the recorded travel time. As the environ-  
<sup>400</sup> mental and ray filtering method become better representations of the real ocean, the lower  
<sup>401</sup> the expected mismatch is between the implied and estimated effective sound speeds.

<sup>402</sup> The various sound speed inputs—isovelocity aside—not only modify the predicted effec-  
<sup>403</sup> tive sound speed, as seen by the colored vertical offsets, but often classify a distinct number  
<sup>404</sup> of bounces. HYCOM sees the most direct and one bounce multipath structures, lending a  
<sup>405</sup> bias for faster speeds; the weighted SSP sees the most double and triple bounces, favoring  
<sup>406</sup> slower speeds; the baseline sound speed exists in between. Very rarely is the multipath  
<sup>407</sup> structure classified as a direct path, i.e., where the NB defaults to the MB prediction. In  
<sup>408</sup> fact, the higher the multipath classification, the more accurate the sound speed prediction  
<sup>409</sup> is, likely driven by a tighter or even sparser bundle of rays. Discontinuities in multipath  
<sup>410</sup> classification provide initial evidence for its importance to a smoothly varying group velocity,

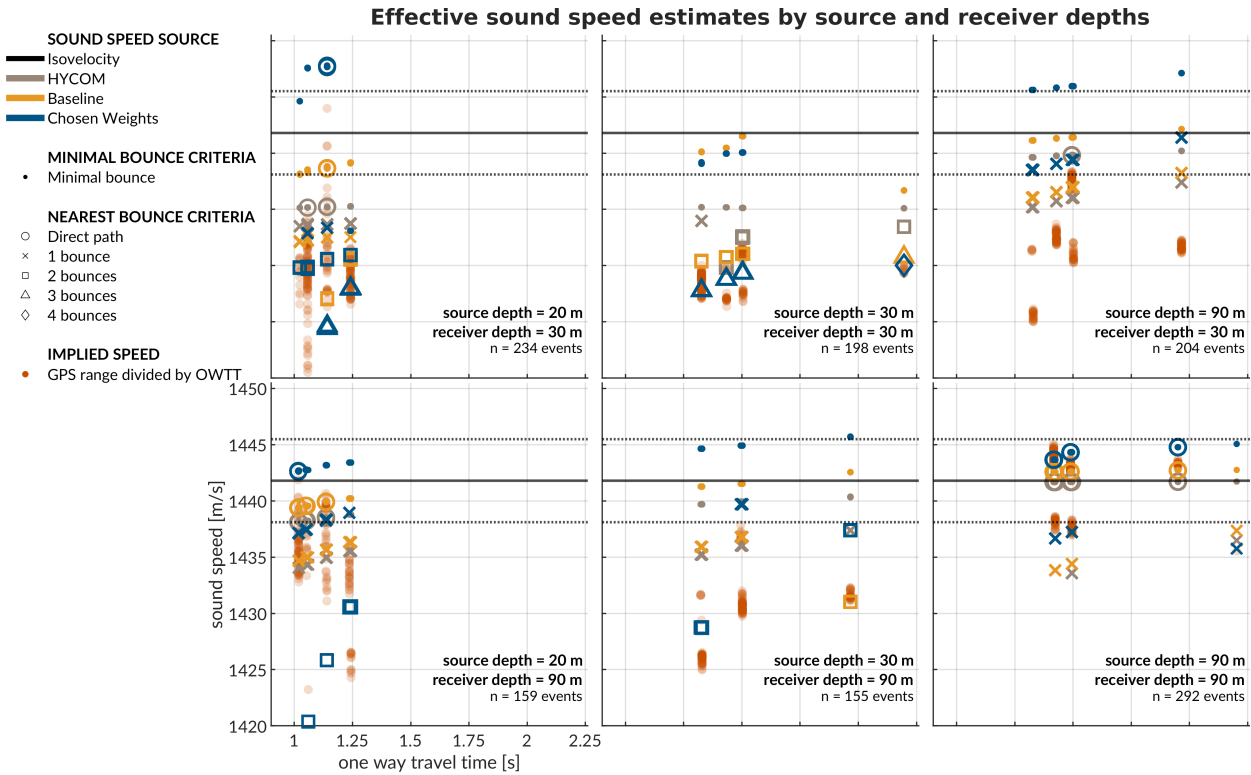


FIG. 9. A post-processing comparison of effective sound speed predictions for all beacon-to-beacon events. The rows share receiver depth; the columns share source depth. The recorded travel time is on the x-axis and the predicted effective sound speed is on the y-axis. The sound speed source is indicated by color. The isovelocity is shown as the mean  $\pm$  the standard deviation. The minimal and nearest bounce criterion are distinguished by different marker shapes, compared to the separately colored red dots showing the implied calculation.

as shown in the cluster of 30 to 30 m transmissions in Fig. 9, where HYCOM jumps from one to two classified bounces amidst the baseline SSP and weighted SSP smoothly increasing while consistently seeing two and three classified bounces, respectively. Of course, the prediction deteriorates with cross-layer transmissions across the duct, but not to the same degree at which eigenrays could not be found for the weighted SSP in section III C. The

<sup>416</sup> evidence suggests that the grid based method provides a useful amount of redundancy to  
<sup>417</sup> resolve similar enough eigenrays.

<sup>418</sup> It is useful to think about in what case the isovelocity—or any isovelocity framing—would  
<sup>419</sup> have been appropriate. The transmissions from shallow to shallow receiver may have  
<sup>420</sup> matched the default configuration of 1430 m/s. The isovelocity contrived for this paper,  
<sup>421</sup> 1441.8 m/s, best matches the transmissions from 90 to 90 m. The one from [Graupe \*et al.\*](#)  
<sup>422</sup> ([2019](#)), 1450 m/s, would have had a systemic overestimation. In addition, over the course  
<sup>423</sup> of the four day experiment, the local maxima of the Beaufort Lens changed from roughly  
<sup>424</sup> 1447 m/s at 40 m to 1442 m/s at 60 m. Given that implied sound speeds just for beacon-  
<sup>425</sup> to-beacon events span 1420 to 1445 m/s, it is safe to say that a nominal sound speed would  
<sup>426</sup> sacrifice pseudorange accuracy somewhere, and that an adaptive approach is necessary even  
<sup>427</sup> for short and/or small scale operations in the Beaufort Lens.

### <sup>428</sup> C. Pseudorange error metrics

<sup>429</sup> Pseudorange estimation plays an important role in trilateration. Fig. [10](#) shows the  
<sup>430</sup> directional pseudorange error “footprints” for the four sound speed inputs with the NB  
<sup>431</sup> approach, separated by source and receiver depth configurations.

<sup>432</sup> The weighted SSP range error generally has the smallest and most zero-centered footprint.  
<sup>433</sup> The one case it does not is for the source-receiver pairings between 30 and 90 m in depth. The  
<sup>434</sup> increased error for these is most likely driven by the computational artifacts encountered  
<sup>435</sup> when propagating through the steep sound speed gradients of the lens and through the

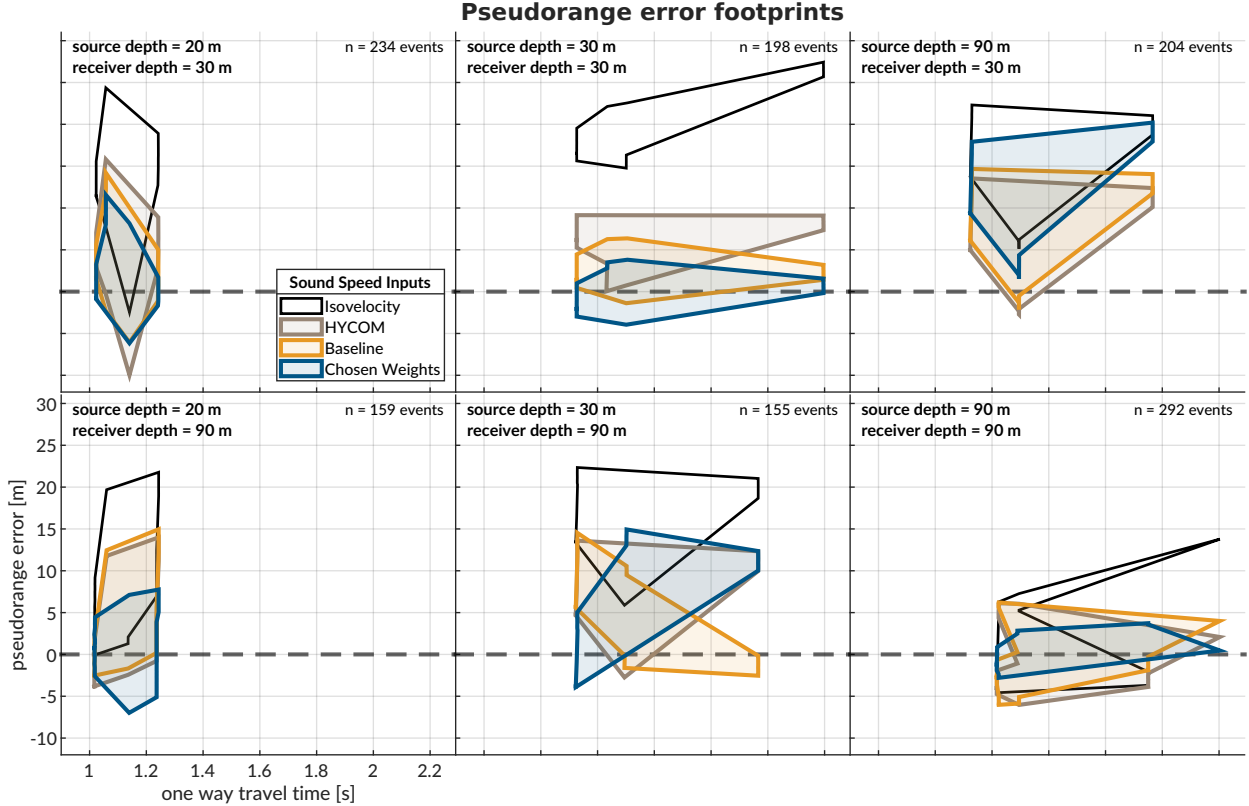


FIG. 10. The post-processed pseudorange error; the rows share receiver depth; the columns share source depth. The dashed gray line shows no error. The shaded region connects the range performance across all events.

<sup>436</sup> shadow zone. All other source depth pairings are significantly improved using the chosen  
<sup>437</sup> weights compared to HYCOM or the baseline.

<sup>438</sup> When using a linear scaling to convert travel time into range, any offset between the  
<sup>439</sup> assumed sound speed and the horizontal group velocity produces unconstrained error with  
<sup>440</sup> increasing receiver distance, whereas an adaptive estimate would exhibit no such trend. This  
<sup>441</sup> is easily observed in the same-layer links, i.e., 30 to 30 m and 90 to 90 m. In cross-layer  
<sup>442</sup> links, the isovelocity does not perform better but tends to exaggerate or flip the footprint  
<sup>443</sup> created adaptively.

444 The improvement from MB to NB is most evident for the data-driven sound speed;  
445 while the HYCOM SSP improves from a median absolute range error of 6.41 to 4.61 m,  
446 the baseline SSP improves from 10.30 to 2.27 m, and the weighted SSP improves from  
447 13.28 to 2.12 m. In comparison, the isovelocit y has a median error of 13.09 m. The order  
448 of magnitude improvement in the ducted SSPs demonstrate the effectiveness of the NB  
449 algorithm exploiting the observed multipath conditions.

450 There is one example that helpfully illustrates the improvement brought upon by bounce  
451 classification. For transmissions between North and South at 30 m, the OWTT spread is  
452 2.1958 to 2.1963 s; the GNSS-tracked distance is 3138.54 to 3140.87 m; and the implied  
453 effective sound speed is 1429.3 to 1430.1 m/s. For these transmissions, the weighted SSP  
454 and the MB approach produce a pseudorange error of -1491 m, as the effective sound speed  
455 predicted by the minimum bounce criteria is dominated by bottom bounce arrivals with  
456 much greater travel times. The NB approach categorizes this same record as a quadruple  
457 surface bounce, reducing the pseudorange error to less than a meter. Comparatively, the NB  
458 approach for HYCOM and the baseline SSP produce pseudorange errors of 8.30 and 2.39  
459 m, respectively. There is strong evidence to suggest that the sound speed and multipath  
460 fidelity codependently improve localization accuracy.

<sup>461</sup> **V. TRILATERATION FOR ICEX20 FIELD DATA**

<sup>462</sup> To overcome potentially intermittent acoustic communication, the operational paradigm  
<sup>463</sup> of the ICNN computes corrections relative to the trilaterated position estimates transmitted  
<sup>464</sup> by the vehicle, rather than transmitting the updated positions themselves. The reliability  
<sup>465</sup> of the correction is directly linked to how accurately the travel time measurements are  
<sup>466</sup> converted to pseudoranges. This section aims to resolve that tension by reevaluating the  
<sup>467</sup> trilateration results with respect to the MB and NB algorithms. The MB/NB effective  
<sup>468</sup> speed predictions were tracked independently for each source-receiver pair; although the  
<sup>469</sup> sound speed was expected to be locally smooth near a given receiver, no such assumption  
<sup>470</sup> was enforced between distinct acoustic links.

<sup>471</sup> **A. Re-positioning beacon to beacon events**

<sup>472</sup> When the beacons ran as virtual vehicles, the ICNN did not have access to that buoy's  
<sup>473</sup> GPS data stream except for what was sent via digital acoustic message. The static nature  
<sup>474</sup> of the experiment means that the initial estimate transmitted to the ICNN was in fact a  
<sup>475</sup> ground truth position. Therefore, a distribution of corrections from the ICNN, as shown in  
<sup>476</sup> Fig. 11, reflects positioning accuracy. The NB clearly outperforms the MB, with almost 80%  
<sup>477</sup> of the corrections below 6 meters and the median within the deployed GNSS puck precision  
<sup>478</sup> of 3 meters. By contrast, the MB shows roughly 20% within the GNSS puck precision,  
<sup>479</sup> and separate peaks from 9–12 meters and 21–27 meters. This trimodal nature reflects the  
<sup>480</sup> distribution of reflections on the ice surface.

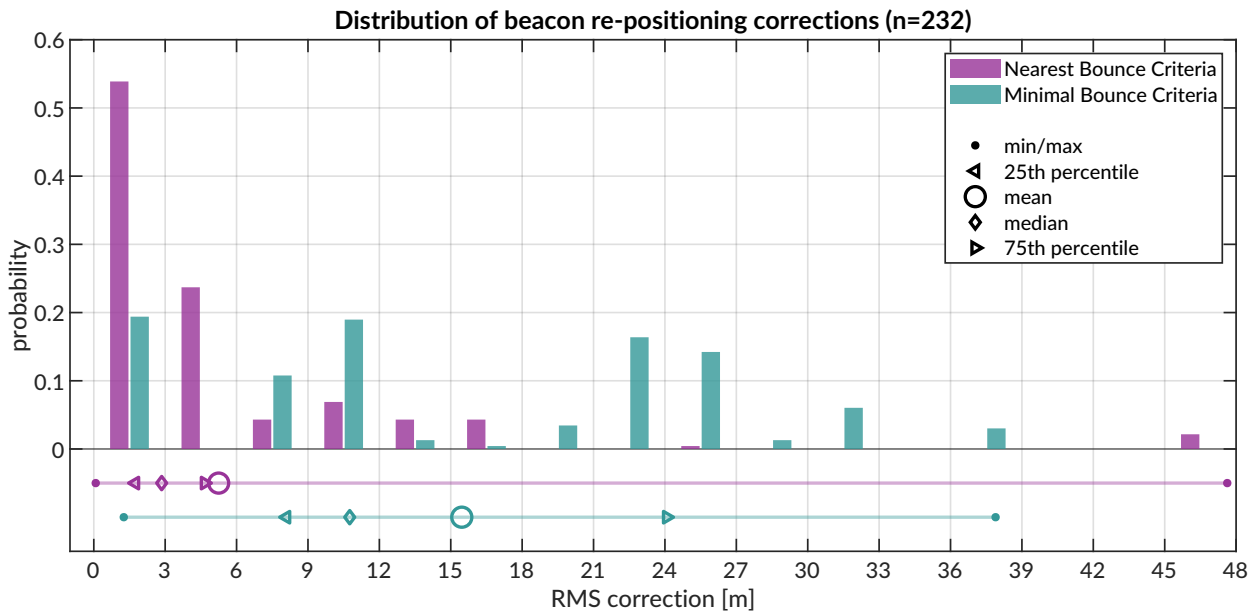


FIG. 11. Trilateration events; however, 264 entries are 2-beacon solutions, 22 are 3-beacon, and 2 are 4-beacon. When limited to only two ranging circles, the trilateration chooses the closer of the two intersection points. The x-axis is cut off at the upper limit for the NB algorithm.

481 In several events, the MB is unable to accurately estimate the effective sound speed for  
 482 one of the acoustic links, leading to a large positioning error. The NB, however, better  
 483 resolves an approximation of the acoustic path. For example, in some trilateration solutions  
 484 for the Eastern buoy, the MB shows a correction of more than a kilometer; the NB is two  
 485 orders of magnitudes less.

486 **B. Re-navigating AUV *Macrura***

487 Up to this point, pseudorange estimation and localization have been evaluated on GPS-  
 488 linked beacon-to-beacon connections to validate the NB algorithm. This analysis ports the  
 489 MB and NB algorithms to re-navigate the AUV *Macrura*.

490 In comparison to the modem experiment, the AUV data clearly exhibit instances where  
491 a receiver detects the same transmission more than once. This is not surprising considering  
492 the complex multipath provided by the Beaufort Lens. The 11 hour vehicle mission con-  
493 tains 3,260 transmissions, 12,938 total detections, and 4,704 successful receptions. Allowing  
494 receptions with PSK errors would almost double the number of recorded multipath arrivals  
495 exploited for positioning, if a real-time solution could correctly parse paths from different  
496 arrivals in the same thirty-second cycle. Thus it remains a future endeavor to explore how  
497 failure mode information from acoustic modems could be used to identify unsuccessful but  
498 otherwise trustworthy arrivals to augment trilateration samples.

499 The following performance analysis is constrained to what the vehicle acted on in real-  
500 time. AUV *Macrura* and the ICNN ran an adaptive depth behavior to maintain acoustic  
501 communication on the insight that cross-layer links were more likely to fail than same-layer  
502 ones. Accordingly, the vehicle dove deeper than 50 meters about 20% of the time it was  
503 underway.

504 In contrast to the modem tests, where position correction illustrated re-positioning ac-  
505 curacy, the re-navigation corrections are less valuable in the absence of GNSS ground truth.  
506 The correction magnitude necessarily depends on the vehicle's internal navigation estimate,  
507 which is prone to larger errors from sensor drifts, ocean currents, and other error not cap-  
508 tured in the hydrodynamic model. Thus, larger corrections are not necessarily indicative of  
509 worse performance. Navigation accuracy is better described by trilateration error, the RMS  
510 of the remaining pseudorange errors from each acoustic link.

511 Fig. 12 shows the correction magnitudes and trilateration errors for events with three or  
 512 more receptions during AUV operations. Whereas the MB has a fairly bimodal nature, with  
 513 peaks centered around 10–15 and 35–40 m, the NB favors smaller corrections, from 5–20 m,  
 514 and has a long tail. The distribution of corrections are much larger than the distribution  
 515 of RMS error. It is apparent that, while both methods are quite successful, there is strong  
 516 evidence that the NB achieves single meter accuracy.

### 517 C. Investigating potential GNSS noise

518

519 The fact that the bulk of the best performing re-navigation error exists within the preci-  
 520 sion of the GNSS unit deployed invites a further look into GNSS noise. In the Arctic, GNSS  
 521 performance worsens due to poor constellation coverage, larger ionospheric effects, and mul-  
 522 tipath interference (Gwal and Jain, 2011; Jung *et al.*, 2018; National Research Council, 2011;  
 523 Reid *et al.*, 2016; Swarlund *et al.*, 2016; Themens *et al.*, 2015). Radio infrastructure that  
 524 provides position corrections and references does not regularly extend to polar regions. The  
 525 effect is minor for surface platform navigation —roughly 15 m of horizontal precision has  
 526 been displayed at the North Pole—but is significant enough to register against the modem’s  
 527 detected travel times. Fig. 13 zooms in on the GNSS and OWTT noise relative to the ice  
 528 movement for two pairs of modem buoy connections. The two panels indicate the GPS noise  
 529 as  $\delta R = \sqrt{\delta x^2 + \delta y^2}$  and temporal drift,  $\delta t$ , relative to the median OWTT recorded between  
 530 the two modems. The dashed line is scaled by a group velocity of 1440 m/s, such that if

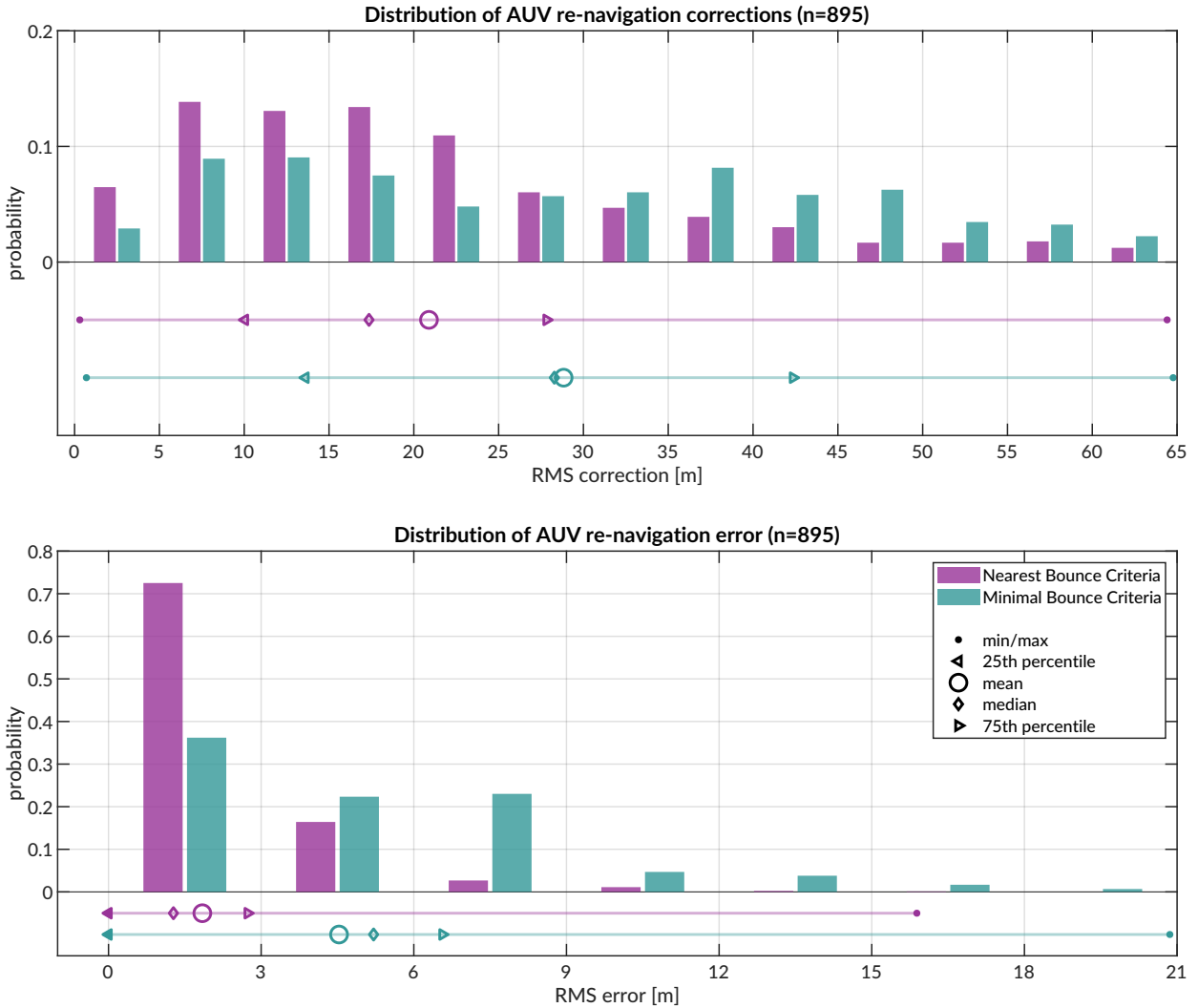


FIG. 12. Distribution of vehicle re-navigation corrections (top) and error (bottom) computed in post-processing for the Minimal and Nearest Bounce Criterion.

531 there were ideal sensor measurements with no drift, all events should exist on or near the  
 532 line.

533 The left panel shows the connections between the North and East buoys. The clusters  
 534 scaling along the 1440 m/s guideline suggest relative ice movement picked up by both GNSS  
 535 and OWTT. But the vertical distribution across many arrival time bands is indicative of

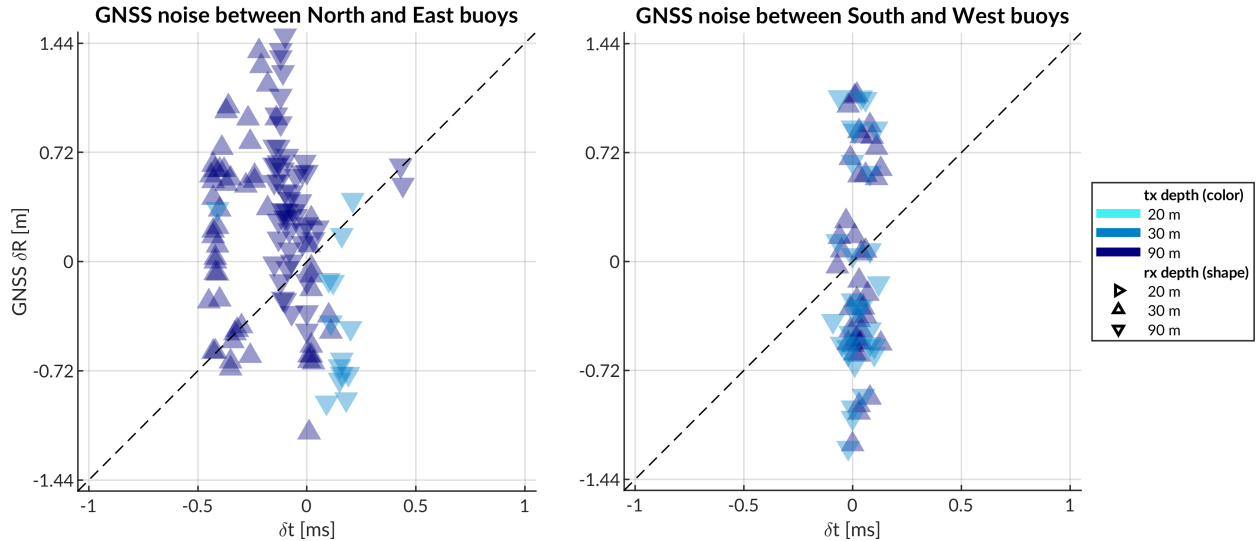


FIG. 13. A comparison of GPS noise (y-axis) versus OWTT drift (x-axis) for corners of the ICNN network with different source depths.

the GNSS fluctuations in precision, or noise. Some minor offsets between these vertical bands relate to different operational configurations of source and receiver depth. The idea of GNSS noise relative to OWTT is further indicated by events between two other buoys, South and West. The relatively thin time window suggests these buoys are moving in a more rigid ice floe and that there is minimal impact by source and receiver depth on the spread of OWTT. Yet, the vertical distribution, spanning almost 4 meters, cannot be explained by time differentials due to acoustic scattering, multipath, and/or environmental microstructure. This conclusion corroborates the vertical spread of implied effective speeds in Fig. 9.

545 **VI. DISCUSSION**

546 Underwater navigation research is broadly motivated by acquiring GNSS-like navi-  
 547 gation in GNSS-denied conditions. Accurate range estimation is essential to mitigating error.  
 548 Current approaches for underwater acoustic navigation simplify the non-linear relationship  
 549 between a SSP and timefronts with a deterministic sound speed. Thus, the conversion of  
 550 travel time into distance can be pre-conditioned for error and error growth over the course  
 551 of a vehicle mission. This work introduces a lightweight stochastic prediction of an effec-  
 552 tive speed along the acoustic path between source and receiver, retooling arrival methods  
 553 generally deemed too complex or labor intensive for real-time. We assume that the effec-  
 554 tive sound speed would be a locally smoothly varying function with respect to operational  
 555 conditions—horizontal and vertical differences and rate of difference between source and re-  
 556 ceiver. The field-tested approach, the minimal bounce criteria, facilitated a successful AUV  
 557 recovery in a total ice-covered, double ducted environment. The accuracy of the MB was  
 558 validated against GPS-linked beacon-to-beacon communications. Given a consistent bias  
 559 towards overestimation, an improved algorithm, the nearest bounce criteria, was developed  
 560 on the insight that multipath structure may play an outsized role in maintaining a smoothly  
 561 varying effective sound speed. The NB was developed with field data and reevaluated on  
 562 vehicle data, achieving a position accuracy and precision that compares with that of the  
 563 deployed GNSS puck.

564 A key insight for both approaches was seeking an eigenray ensemble around an estimated  
 565 location instead of seeking to unambiguously match arrivals. The ensemble diversified the

566 simulated multipath possibilities to better capture the actual multipath recorded. In this  
567 way, the solution exploits multipath, generally viewed as a source of uncertainty, as a new  
568 dimension of information to improve localization accuracy. Based on the navigation and re-  
569 navigation results of our AUV deployment in the ice-covered Beaufort Sea, we conclude that  
570 embedding a model-aided prediction of the effective sound speed has an outsized benefit  
571 to minimizing trilateration error, and that our approach sufficiently resolves the acoustic  
572 timefronts for an unpredictable, complex propagation environment like the double ducted  
573 Beaufort Lens.

574 There are many avenues through which this approach can be further refined and tested for  
575 field operations. Amongst them is defining the uncertainty grid for BELLHOP via stochastic  
576 or data-driven measures such as the distance traveled by the AUV between ICNN updates  
577 or the magnitude of the position corrections by the ICNN. Another is to entirely remove the  
578 seeded range and instead rely on the submerged asset's depth and recorded OWTT to find  
579 high probability fields in range.

580 The relatively simple nature of this approach suggests it is transferable to other envi-  
581 ronments, spatio-temporal scales, and platforms. While it is likely a particular quirk of  
582 the Beaufort Lens that filtering for reflection alone can produce a horizontal effective speed  
583 that compensates for ray refraction and reflection, the algorithm can be reconditioned to  
584 filter against other metrics, like number of turning points, to create a more diverse and in-  
585 formed set of multipath timefronts. Though the majority of re-navigation results are within  
586 single-meter accuracy, future work can examine how constellations of more LBL beacons  
587 can extend the operational domain without adding an undesirable amount of error. One

588 possibility is that, during a mission, ICNN-like LBL implementations use a comparison of  
589 the GNSS self-position and acoustic positioning to invert for the ocean volume, linking how  
590 vertical and horizontal sound speed structure impact transmission integrity. A fast tomo-  
591 graphic estimate (Deffenbaugh, 1997; Elisseeff *et al.*, 2002), along with its uncertainty, could  
592 be continuously communicated to assets underway to maintain contact or enable adaptive  
593 sampling. In this sense navigation and tomography converge on the same set of compo-  
594 nent technologies—position estimation, sound speed parameterization estimation, ray path  
595 identification, and vehicle path optimization.

596 Spatio-temporal variability is a serious challenge for accurate real-time ranging. On  
597 one hand, the effectiveness of eigenray filtering algorithm is likely only challenged by the  
598 valid operational scales of a range independent propagation environment. Longer range  
599 experiments may provide more time for eigenray filtering. A bootstrapping approach that  
600 filters eigenrays for several randomly generated internal wave spectrums may compensate  
601 for otherwise unknowable spatio-temporal variability. The model-aided component to the  
602 eigenray filtering is compatible with vertical slices from any physically driven ocean model.  
603 But in the long run, more accurate and higher resolution global circulation models are  
604 needed to properly resolve features that alter ducted propagation at the scales discernible  
605 to an acoustic modem. Through-the-sensor methods can resolve local features but would  
606 require a degree of information sharing not readily supported on the acoustic channel for  
607 large scale variability. But addressing the spatial and temporal scales of what can be solved  
608 deterministically and what must be solved stochastically imposes a resolution constraint  
609 that is at odds with computational overhead for real-time operations. Resolving features

610 inaccurately, or with a false sense of confidence, could be more harmful than contextualizing  
611 the limitations of a range independent propagation over realistic bathymetry. Given that  
612 AUV operations are often on smaller spatial and temporal scales, the added benefit of an  
613 ocean model is quite small, and for features like the Beaufort Lens, not well resolved.

614 The methods involved in this paper include open source software projects ([Benjamin \*et al.\*, 2010](#),  
615 [Schneider \*et al.\*, 2015](#); [Schneider and Schmidt, 2010](#)) that are platform agnostic. Large  
616 AUVs, often large enough to support long duration and/or deep sea missions, would benefit  
617 from including diurnal or tidal effects for ranging. Gliders, though generally low power and  
618 memory, have been equipped with acoustic modems. Their inability to maintain position  
619 within a region of reliable acoustic path makes the impact of an environmentally adaptive  
620 pseudorange estimation disproportionately positive. The exact adjustments to the ensemble  
621 eigenray filtering are predicated on the expected sound speed conditions and acoustic arrival  
622 structure; the problem is ripe for other simulation testbeds or machine learning methods.  
623 The continued development of embedded acoustic processing on heterogenous platforms is  
624 fundamental to support a universal underwater navigation scheme comparable to GNSS.

625 **ACKNOWLEDGMENTS**

626 We acknowledge the significant operational effort spearheaded by the LAMSS ICEX20  
 627 team and all our collaborators. Bhatt was funded by a National Defense, Science, and  
 628 Engineering Graduate Fellowship. This work was supported by the Office of Naval Research  
 629 322-OA under ICEX20 (N00014-17-1-2474) and Task Force Ocean (N00014-19-1-2716).

630

631 Ballard, M. S., Badiey, M., Sagers, J. D., Colosi, J. A., Turgut, A., Pecknold, S., Lin,  
 632 Y.-T., Proshutinsky, A., Krishfield, R., Worcester, P. F., and Dzieciuch, M. A. (**2020**).

633 “Temporal and spatial dependence of a yearlong record of sound propagation from the  
 634 Canada Basin to the Chukchi Shelf,” The Journal of the Acoustical Society of America  
 635 **148**(3), 1663–1680, doi: [10.1121/10.0001970](https://doi.org/10.1121/10.0001970).

636 Barker, L. D., Jakuba, M. V., Bowen, A. D., German, C. R., Maksym, T., Mayer, L.,  
 637 Boetius, A., Dutrieux, P., and Whitcomb, L. L. (**2020**). “Scientific challenges and present  
 638 capabilities in underwater robotic vehicle design and navigation for oceanographic explo-  
 639 ration under-ice,” Remote Sensing **12**(16), 1–31, doi: [10.3390/RS12162588](https://doi.org/10.3390/RS12162588).

640 Bellingham, J. G., Leonard, J. J., Vaganay, J., Goudey, C. A., Atwood, D. K., Consi,  
 641 T. R., Bales, J. W., Schmidt, H., and Chrysostomidis, C. (**1995**). “AUV operations in  
 642 the Arctic,” in *Sea Ice Mechanics and Arctic Modeling Workshop*.

643 Benjamin, M. R., Schmidt, H., Newman, P. M., and Leonard, J. J. (**2010**). “Nested au-  
 644 tonomy for unmanned marine vehicles with MOOS-IvP,” Journal of Field Robotics **27**(6),

- 645 834–875, doi: [10.1002/rob.20370](https://doi.org/10.1002/rob.20370).
- 646 Bhatt, E. C. (2021). “A Virtual Ocean framework for environmentally adaptive, embed-  
647 ded acoustic navigation on autonomous underwater vehicles,” Ph.D. thesis, Woods Hole  
648 Oceanographic Institution, doi: [10.1575/1912/27309](https://doi.org/10.1575/1912/27309).
- 649 Bhatt, E. C., Howard, B., and Schmidt, H. (2022). “An Embedded Tactical Decision Aid  
650 Framework for Environmentally Adaptive Autonomous Underwater Vehicle and Commu-  
651 nication,” IEEE Journal of Oceanic Engineering (accepted).
- 652 Brooke, J. (1981). “ARCS (Autonomous remotely controlled submersible),” in *Proceedings  
653 of the 1981 2nd International Symposium on Unmanned Untethered Submersible Technol-  
654 ogy*, IEEE, Vol. 2, p. 28.
- 655 Chassignet, E. P., Hurlburt, H. E., Smedstad, O. M., Halliwell, G. R., Hogan, P. J.,  
656 Wallcraft, A. J., Baraille, R., and Bleck, R. (2007). “The HYCOM HYbrid Coordinate  
657 Ocean Model data assimilative system,” Journal of Marine Systems **65**(1), 60–83, doi:  
658 [10.1016/j.jmarsys.2005.09.016](https://doi.org/10.1016/j.jmarsys.2005.09.016).
- 659 Chen, R., Poulsen, A., and Schmidt, H. (2019). “Spectral, spatial, and temporal character-  
660 istics of underwater ambient noise in the Beaufort Sea in 1994 and 2016,” The Journal of  
661 the Acoustical Society of America **145**(2), 605–614, doi: [10.1121/1.5088601](https://doi.org/10.1121/1.5088601).
- 662 Chen, R., and Schmidt, H. (2020). “Temporal and spatial characteristics of the Beaufort  
663 Sea ambient noise environment,” The Journal of the Acoustical Society of America **148**(6),  
664 3928–3941, doi: [10.1121/10.0002955](https://doi.org/10.1121/10.0002955).
- 665 Claus, B., Kepper, J. H., Suman, S., and Kinsey, J. C. (2018). “Closed-loop one-way-travel-  
666 time navigation using low-grade odometry for autonomous underwater vehicles,” Journal

- 667 of Field Robotics **35**(4), 421–434, doi: [10.1002/rob.21746](https://doi.org/10.1002/rob.21746).
- 668 Deffenbaugh, M. (1997). “Optimal Ocean Acoustic Tomography and Navigation with Mov-
- 669 ing Sources,” Phd thesis.
- 670 Deffenbaugh, M., Bellingham, J. G., and Schmidt, H. (1996a). “The relationship between
- 671 spherical and hyperbolic positioning,” in *OCEANS 96 MTS/IEEE Conference Proceedings*.
- 672 *The Coastal Ocean - Prospects for the 21st Century*, Vol. 2, pp. 590–595, doi: [10.1109/OCEANS.1996.568293](https://doi.org/10.1109/OCEANS.1996.568293).
- 673
- 674 Deffenbaugh, M., Schmidt, H., and Bellingham, J. G. (1996b). “Acoustic positioning in a
- 675 fading multipath environment,” in *OCEANS 96 MTS/IEEE Conference Proceedings*, Vol.
- 676 2, pp. 596—600, doi: [10.1109/OCEANS.1996.568294](https://doi.org/10.1109/OCEANS.1996.568294).
- 677 Duda, T. F., Morozov, A. K., Howe, B. M., Brown, M. G., Speer, K., Lazarevich, P.,
- 678 Worcester, P. F., and Cornuelle, B. D. (2006). “Evaluation of a Long-Range Joint Acoustic
- 679 Navigation Thermometry System,” in *OCEANS 2006*, pp. 1–6, doi: [10.1109/OCEANS.2006.306999](https://doi.org/10.1109/OCEANS.2006.306999).
- 680
- 681 Duda, T. F., Zhang, W. G., and Lin, Y.-T. (2021). “Effects of Pacific Summer Water layer
- 682 variations and ice cover on Beaufort Sea underwater sound ducting,” *J. Acoust. Soc. Am.*
- 683 21.
- 684 Duda, T. F., Zhang, W. G., Lin, Y.-T., and Newhall, A. E. (2019). “Long-range sound
- 685 propagation in the Canada Basin,” .
- 686 Elisseeff, P., Schmidt, H., and Xu, W. (2002). “Ocean acoustic tomography as a data
- 687 assimilation problem,” *IEEE Journal of Oceanic Engineering* **27**(2), 275–282, doi: [10.1109/JOE.2002.1002482](https://doi.org/10.1109/JOE.2002.1002482).
- 688

- 689 Eustice, R. M., Whitcomb, L. L., Singh, H., and Grand, M. (2006). “Recent advances in  
690 synchronous-clock one-way-travel-time acoustic navigation,” in *Oceans 2006*, IEEE, pp.  
691 1–6, doi: [10.1109/OCEANS.2006.306931](https://doi.org/10.1109/OCEANS.2006.306931).
- 692 Eustice, R. M., Whitcomb, L. L., Singh, H., and Grund, M. (2007). “Experimental Re-  
693 sults in Synchronous-Clock One-Way-Travel-Time Acoustic Navigation for Autonomous  
694 Underwater Vehicles,” in *Proceedings 2007 IEEE International Conference on Robotics  
and Automation*, pp. 4257–4264, doi: [10.1109/ROBOT.2007.364134](https://doi.org/10.1109/ROBOT.2007.364134).
- 695 Fossum, T. O., Norgren, P., Fer, I., Nilsen, F., Koenig, Z. C., and Ludvigsen, M. (2021).  
696 “Adaptive Sampling of Surface Fronts in the Arctic Using an Autonomous Underwater  
697 Vehicle,” *IEEE Journal of Oceanic Engineering* **46**(4), 1155–1164, doi: [10.1109/JOE.2021.3070912](https://doi.org/10.1109/JOE.2021.3070912).
- 700 Freitag, L., Ball, K., Partan, J., Koski, P., and Singh, S. (2016). “Long range acoustic com-  
701 munications and navigation in the Arctic,” in *OCEANS 2015 - MTS/IEEE Washington*,  
702 IEEE, pp. 1–5, doi: [10.23919/oceans.2015.7401956](https://doi.org/10.23919/oceans.2015.7401956).
- 703 Graupe, C. E., Van Uffelen, L. J., Webster, S. E., Worcester, P. F., and Dzieciuch, M. A.  
704 (2019). “Preliminary results for glider localization in the Beaufort Duct using broadband  
705 acoustic sources at long range,” in *OCEANS 2019 MTS/IEEE Seattle, OCEANS 2019*,  
706 IEEE, pp. 1–6, doi: [10.23919/OCEANS40490.2019.8962637](https://doi.org/10.23919/OCEANS40490.2019.8962637).
- 707 Gwal, A., and Jain, A. (2011). “GPS scintillation studies in the arctic region during the  
708 first winter-phase 2008 Indian Arctic Expedition,” *Polar Science* **4**(4), 574–587, doi: [10.1016/j.polar.2010.08.001](https://doi.org/10.1016/j.polar.2010.08.001).

- 710 Hayes, D. R., and Morison, J. H. (2002). “Determining turbulent vertical velocity, and  
 711 fluxes of heat and salt with an autonomous underwater vehicle,” *Journal of Atmospheric*  
 712 and *Oceanic Technology* **19**(5), 759–779.
- 713 Howe, B. M., Miksis-Olds, J., Rehm, E., Sagen, H., Worcester, P. F., and Haralabus, G.  
 714 (2019). “Observing the Oceans Acoustically,” *Frontiers in Marine Science* **6**(JUL), 1–22,  
 715 doi: [10.3389/fmars.2019.00426](https://doi.org/10.3389/fmars.2019.00426).
- 716 Jackson, E. (1983). “Autonomous remotely controlled submersible ”ARCS”,” in *Proceedings*  
 717 of the 1983 3rd International Symposium on Unmanned Untethered Submersible Technol-  
 718 ogy, IEEE, Vol. 3, pp. 77–88.
- 719 Jakuba, M. V., Roman, C. N., Singh, H., Murphy, C., Kunz, C., Willis, C., Sato, T.,  
 720 and Sohn, R. A. (2008). “Long-baseline acoustic navigation for under-ice autonomous  
 721 underwater vehicle operations,” *Journal of Field Robotics* **25**(11-12), 861–879, doi: <https://doi.org/10.1002/rob.20250>.
- 723 Jung, T. S., Hegel, T. M., Bentzen, T. W., Egli, K., Jessup, L., Kienzler, M., Kuba, K.,  
 724 Kukka, P. M., Russell, K., Suitor, M. P., and Tatsumi, K. (2018). “Accuracy and per-  
 725 formance of low-feature GPS collars deployed on bison *Bison bison* and caribou *Rangifer*  
 726 *tarandus*,” *Wildlife Biology* **2018**(1), doi: [10.2981/wlb.00404](https://doi.org/10.2981/wlb.00404).
- 727 Kepper, J. H., Claus, B. C., and Kinsey, J. C. (2017). “MEMS IMU and one-way-travel-  
 728 time navigation for autonomous underwater vehicles,” in *OCEANS 2017 - Aberdeen*, IEEE,  
 729 Aberdeen, UK, pp. 1–9, doi: [10.1109/OCEANSE.2017.8084842](https://doi.org/10.1109/OCEANSE.2017.8084842).
- 730 Krishfield, R., Toole, J., Proshutinsky, A., and Timmermans, M. L. (2008). “Automated  
 731 ice-tethered profilers for seawater observations under pack ice in all seasons,” *Journal of*

- 732 Atmospheric and Oceanic Technology **25**(11), 2091–2105, doi: [10.1175/2008JTECH0587](https://doi.org/10.1175/2008JTECH0587).
- 733 1.
- 734 Kukulya, A., Plueddemann, A., Austin, T., Stokey, R., Purcell, M., Allen, B., Littlefield, R.,
- 735 Freitag, L., Koski, P., Gallimore, E., Kemp, J., Newhall, K., and Pietro, J. (2010). “Under-
- 736 ice operations with a REMUS-100 AUV in the Arctic,” in *2010 IEEE/OES Autonomous*
- 737 *Underwater Vehicles, AUV 2010*, IEEE, pp. 1–8, doi: [10.1109/AUV.2010.5779661](https://doi.org/10.1109/AUV.2010.5779661).
- 738 Kunz, C., Murphy, C., Camilli, R., Singh, H., Bailey, J., Eustice, R., Jakuba, M., Nakamura, K. I., Roman, C., Sato, T., Sohn, R. A., and Willis, C. (2008). “Deep sea underwater
- 739 robotic exploration in the ice-covered arctic ocean with AUVs,” in *2008 IEEE/RSJ Interna-*
- 740 *tional Conference on Intelligent Robots and Systems, IROS*, IEEE, pp. 3654–3660, doi:
- 741 [10.1109/IROS.2008.4651097](https://doi.org/10.1109/IROS.2008.4651097).
- 742
- 743 Light, R. D., and Morison, J. (1989). “The Autonomous Conductivity-Temperture Vehicle:
- 744 First in the Seashuttle Family of Autonomous Underwater Vehicle’s for Scientific Pay-
- 745 loads,” in *Proceedings OCEANS*, Vol. 3, pp. 793–798, doi: [10.1109/OCEANS.1989.586683](https://doi.org/10.1109/OCEANS.1989.586683).
- 746 Litvak, A. G. (2015). “Acoustics of the deepwater part of the Arctic Ocean and of Russia’s
- 747 Arctic shelf,” *Herald of the Russian Academy of Sciences* **85**(3), 239–250, doi: [10.1134/S1019331615030144](https://doi.org/10.1134/S1019331615030144).
- 748
- 749 Mikhalevsky, P. N., Sperry, B. J., Woolfe, K. F., Dzieciuch, M. A., and Worcester, P. F.
- 750 (2020). “Deep ocean long range underwater navigation,” *The Journal of the Acoustical*
- 751 *Society of America* **147**(4), 2365–2382, doi: [10.1121/10.0001081](https://doi.org/10.1121/10.0001081).
- 752 National Research Council (2011). *National Security Implications of Climate Change for*
- 753 *U.S. Naval Forces* (National Academies Press, Washington, D.C.).

- 754 Norgren, P., Lubbad, R., and Skjetne, R. (2014). “Unmanned underwater vehicles in Arctic  
755 operations,” in *Proceedings of the 22nd IAHR International Symposium on Ice. Singapore,*  
756 pp. 89–101.
- 757 Paull, L., Saeedi, S., Seto, M., and Li, H. (2014). *AUV Navigation and Localization: A*  
758 *Review*, **39**, pp. 131–149.
- 759 Plueddemann, A. J., Kukulya, A. L., Stokey, R., and Freitag, L. (2012). “Autonomous  
760 Underwater Vehicle Operations Beneath Coastal Sea Ice,” IEEE/ASME Transactions on  
761 Mechatronics **17**(1), 54–64, doi: [10.1109/TMECH.2011.2174798](https://doi.org/10.1109/TMECH.2011.2174798).
- 762 Porter, M. B. (2011). “The bellhop manual and user’s guide: Preliminary draft,” .
- 763 Poulsen, A. J., and Schmidt, H. (2017). “Acoustic noise properties in the rapidly changing  
764 Arctic Ocean,” Proceedings of Meetings on Acoustics (28), 1–10, doi: [10.1121/2.0000552](https://doi.org/10.1121/2.0000552).
- 765 Randeni, S., Schneider, T., and Schmidt, H. (2020). “Construction of a high-resolution  
766 under-ice AUV navigation framework using a multidisciplinary virtual environment,” in  
767 *2020 IEEE/OES Autonomous Underwater Vehicles Symposium, AUV 2020*, IEEE, pp.  
768 1–7, doi: [10.1109/AUV50043.2020.9267950](https://doi.org/10.1109/AUV50043.2020.9267950).
- 769 Randeni, S., Schneider, T., Schmidt, H., Bhatt, E., and Viquez, O. (2021). “A high-  
770 resolution AUV navigation framework with integrated communication and tracking for  
771 under-ice deployments,” Field Robotics (in review).
- 772 Reid, T., Walter, T., Blanch, J., and Enge, P. (2016). “GNSS Integrity in The Arctic,”  
773 Navigation **63**(4), 469–492, doi: [10.1002/navi.169](https://doi.org/10.1002/navi.169).
- 774 Rossby, T., Dorson, D., and Fontaine, J. (1986). “The RAFOS System,” Journal of  
775 Atmospheric and Oceanic Technology **3**(4), 672–679, doi: [10.1175/1520-0426\(1986\)003;4-672.TRAFSY.01200833.0240](https://doi.org/10.1175/1520-0426(1986)003;4-672.TRAFSY.01200833.0240)

776 003<0672:TRS>2.0.CO;2.

777 Rypkema, N. R., Fischell, E. M., and Schmidt, H. (2017). “One-Way Travel-Time Inverted  
778 Ultra-Short Baseline Localization for Low-Cost Autonomous Underwater Vehicles,” in *2017*

779 *IEEE International Conference on Robotics and Automation*, Singapore, pp. 4920–4926.

780 Schmidt, H., and Schneider, T. (2016). “Acoustic communication and navigation in the  
781 new Arctic — A model case for environmental adaptation,” 2016 IEEE Third Underwa-  
782 ter Communications and Networking Conference (UComms) 1–4, doi: [10.1109/UComms.2016.7583469](https://doi.org/10.1109/UComms.2016.7583469).

784 Schneider, T., Petillo, S., Schmidt, H., and Murphy, C. (2015). “The dynamic compact  
785 control language version 3,” in *OCEANS 2015-Genova*, IEEE, pp. 1–7.

786 Schneider, T., and Schmidt, H. (2010). “Unified command and control for heterogeneous  
787 marine sensing networks,” *Journal of Field Robotics* **27**(6), 876–889, doi: <https://doi.org/10.1002/rob.20346>.

789 Schneider, T., and Schmidt, H. (2018). “NETSIM: A Realtime Virtual Ocean Hardware-in-  
790 the-loop Acoustic Modem Network Simulator,” in *2018 Fourth Underwater Communica-*

791 *tions and Networking Conference (UComms)*, IEEE, pp. 1–5, doi: [10.1109/UComms.2018.8493188](https://doi.org/10.1109/UComms.2018.8493188).

793 Schneider, T., Schmidt, H., and Randeni, S. (2021). “Self-Adapting Under-Ice Integrated  
794 Communications and Navigation Network,” 2021 Fifth Underwater Communications and  
795 Networking Conference (UComms) 1–5, doi: [10.1109/UComms50339.2021.9598012](https://doi.org/10.1109/UComms50339.2021.9598012).

796 Singh, S., Grand, M., Bingham, B., Eustice, R., Singh, H., and Freitag, L. (2006). “Un-  
797 derwater acoustic navigation with the WHOI Micro-Modem,” in *Oceans 2006*, IEEE, pp.

- 798 1–4, doi: [10.1109/OCEANS.2006.306853](https://doi.org/10.1109/OCEANS.2006.306853).
- 799 Swanlund, D., Maraj, R., Schuurman, N., Hope, R., Donkers, K., Aquin, M., and Rickerby,
- 800 G. (2016). “Gps performance in yukon’s arctic coast,” Geografiska Annaler: Series A,
- 801 Physical Geography **98**(4), 361–368, doi: [10.1111/geoa.12143](https://doi.org/10.1111/geoa.12143).
- 802 Themens, D. R., Jayachandran, P. T., and Langley, R. B. (2015). “The nature of GPS
- 803 differential receiver bias variability: An examination in the polar cap region,” Journal of
- 804 Geophysical Research: Space Physics **120**(9), 8155–8175, doi: [10.1002/2015JA021639](https://doi.org/10.1002/2015JA021639).
- 805 Timmermans, M.-L., and Winsor, P. (2013). “Scales of horizontal density structure in the
- 806 Chukchi Sea surface layer,” Continental Shelf Research **52**, 39–45.
- 807 Toole, J., Krishfield, R., Timmermans, M.-L., and Proshutinsky, A. (2011). “The Ice-
- 808 Tethered Profiler: Argo of the Arctic,” Oceanography **24**(3), 126–135, doi: [10.5670/oceanog.2011.64](https://doi.org/10.5670/oceanog.2011.64).
- 810 Van Uffelen, L. J., Howe, B. M., Nosal, E. M., Carter, G. S., Worcester, P. F., and Dzieci-
- 811 uch, M. A. (2016). “Localization and subsurface position error estimation of gliders using
- 812 broadband acoustic signals at long range,” IEEE Journal of Oceanic Engineering **41**(3),
- 813 501–508, doi: [10.1109/JOE.2015.2479016](https://doi.org/10.1109/JOE.2015.2479016).
- 814 Van Uffelen, L. J., Nosal, E.-M., Howe, B. M., Carter, G. S., Worcester, P. F., Dzieciuch,
- 815 M. A., Heaney, K. D., Campbell, R. L., and Cross, P. S. (2013). “Estimating uncertainty
- 816 in subsurface glider position using transmissions from fixed acoustic tomography sources,”
- 817 The Journal of the Acoustical Society of America **134**(4), 3260–3271, doi: [10.1121/1.4818841](https://doi.org/10.1121/1.4818841).

- 819 Van Uffelen, L. J. V. (2021). “Global Positioning Systems: Over Land and Under Sea,”  
820 *Acoustics Today* **17**(1), 9.
- 821 Webster, S. E., Eustice, R. M., Singh, H., and Whitcomb, L. L. (2009). “Preliminary  
822 deep water results in single-beacon one-way-travel-time acoustic navigation for underwater  
823 vehicles,” in *2009 IEEE/RSJ International Conference on Intelligent Robots and Systems,*  
824 *IROS 2009*, IEEE, pp. 2053–2060, doi: [10.1109/IROS.2009.5354457](https://doi.org/10.1109/IROS.2009.5354457).
- 825 Webster, S. E., Eustice, R. M., Singh, H., and Whitcomb, L. L. (2012). “Advances in single-  
826 beacon one-way-travel-time acoustic navigation for underwater vehicles,” *The International  
827 Journal of Robotics Research* **31**(8), 935–950, doi: [10.1177/0278364912446166](https://doi.org/10.1177/0278364912446166).
- 828 Webster, S. E., Freitag, L. E., Lee, C. M., and Gobat, J. I. (2015). “Towards real-time  
829 under-ice acoustic navigation at mesoscale ranges,” in *Proceedings - IEEE International  
830 Conference on Robotics and Automation*, IEEE, Vol. 2015-June, pp. 537–544, doi: [10.  
831 1109/ICRA.2015.7139231](https://doi.org/10.1109/ICRA.2015.7139231).
- 832 Wu, M., Barmin, M. P., Andrew, R. K., Weichman, P. B., White, A. W., Lavely, E. M.,  
833 Dzieciuch, M. A., Mercer, J. A., Worcester, P. F., and Ritzwoller, M. H. (2019). “Deep  
834 water acoustic range estimation based on an ocean general circulation model: Application  
835 to PhilSea10 data,” *The Journal of the Acoustical Society of America* **146**(6), 4754–4773,  
836 doi: [10.1121/1.5138606](https://doi.org/10.1121/1.5138606).